AGU PUBLICATIONS

JGR

Journal of Geophysical Research: Space Physics

RESEARCH ARTICLE
10.1002/2014JA020111

Key Points:
- The 3-D lunar wake is studied with well-determined solar wind conditions
- The field lines bend in the wake due to flow deceleration
- The 3-D wake structure is investigated by observation data

Correspondence to:
H. Zhang,
hzhang@mail.iggcas.ac.cn

Citation:
Zhang, H., K. K. Khurana, M. G. Kivelson, V. Angelopoulos, W. X. Wan, L. B. Liu, Q.-G. Zong, Z. Y. Pu, Q. Q. Shi, and W. L. Liu (2014), Three-dimensional lunar wake reconstructed from ARTEMIS data, *J. Geophys. Res. Space Physics, 119*, 5220–5243, doi:10.1002/2014JA020111.

Received 22 APR 2014
Accepted 12 JUN 2014
Accepted article online 16 JUN 2014
Published online 24 JUL 2014

Three-dimensional lunar wake reconstructed from ARTEMIS data

H. Zhang[1,2,3], K. K. Khurana[4], M. G. Kivelson[4,5], V. Angelopoulos[4], W. X. Wan[1,2], L. B. Liu[1,2], Q.-G. Zong[6], Z. Y. Pu[6], Q. Q. Shi[7], and W. L. Liu[8]

[1]Key Laboratory of Earth and Planetary Physics, Institute of Geology and Geophysics, Chinese Academy of Sciences, Beijing, China, [2]Beijing National Observatory of Space Environment, Institute of Geology and Geophysics, Chinese Academy of Sciences, Beijing, China, [3]State Key Laboratory of Space Weather, Chinese Academy of Sciences, Beijing, China, [4]Department of Earth and Space Sciences, University of California, Los Angeles, California, USA, [5]Atmospheric, Oceanic and Space Sciences Department, University of Michigan, Ann Arbor, Michigan, USA, [6]School of Earth and Space Sciences, Peking University, Beijing, China, [7]School of Space Science and Physics, Shangdong University at Weihai, Weihai, China, [8]School of Astronautics, Beihang University, Beijing, China

Abstract Data from the two-spacecraft Acceleration, Reconnection, Turbulence and Electrodynamics of the Moon's Interaction with the Sun mission to the Moon have been exploited to characterize the lunar wake with unprecedented fidelity. The differences between measurements made by a spacecraft in the solar wind very near the Moon and concurrent measurements made by a second spacecraft in the near lunar wake are small but systematic. They enabled us to establish the perturbations of plasma density, temperature, thermal, magnetic and total pressure, field, and flow downstream of the Moon to distances of 12 lunar radii (R_M). The wake disturbances are initiated immediately behind the Moon by the diamagnetic currents at the lunar terminator. Rarefaction waves propagate outward at fast MHD wave velocities. Beyond ~6.5 R_M, all plasma and field parameters are poorly structured which suggests the presence of instabilities excited by counter-streaming particles. Inward flowing plasma accelerated through pressure gradient force and ambipolar electric field compresses the magnetic field and leads to continuous increase in magnitude of magnetic perturbations. Besides the downstream distance, the field perturbation magnitude is also a function of the solar wind ion beta and the angle between the solar wind and the interplanetary magnetic field (IMF). Both ion and electron temperatures increase as a consequence of an energy dispersion effect, whose explanation requires fully kinetic models. Downstream of the Moon, the IMF field lines are observed to bulge toward the Moon, which is unexpected and may be caused by a plasma pressure gradient force or/and the pickup of heavy charged dust grains behind the Moon.

1. Introduction

Although there is some evidence that the Moon may have a tenuous atmosphere of charged dust particles extending up to 100 km above the lunar surface [e.g., *Stubbs et al*., 2006] and there are magnetic anomalies located on the Moon surface forming "mini-magnetospheres" [*Halekas et al*., 2008], because it lacks global internal conductivity, an intrinsic magnetic field and a significant atmosphere (ionosphere) [*England et al*., 1968; *Sonett et al*., 1967; *Hoffman et al*., 1973], the Moon is generally treated as an insulator when discussing its interaction with the solar wind in a large (global) scale. When immersed in the supersonic solar wind, the Moon absorbs the incident solar wind but allows the interplanetary magnetic field (IMF) to pass through unaltered [*Lyon et al*., 1967]. If no other process acts, a cylindrical plasma void would form behind the Moon and the magnetic field in that void might be expected to be identical to the IMF. However, the reentry of the ambient plasma into the void does occur downstream of the Moon, which modifies the plasma and magnetic properties in and around the void and produces a complicated structure behind the Moon, generally, referred to as the "lunar wake" [*Colburn et al*., 1967; *Ness et al*., 1967]. The structures of the lunar wake have been extensively explored since the very beginning of the space era in 1960s by missions such as IMP 1, Lunar Explorer 35, and Apollo, and more detailed structures have been discovered by recent missions, such as Lunar Prospector, Wind, Chandrayaan-1, SELENE ChangE, and Acceleration, Reconnection, Turbulence and Electrodynamics of the Moon's Interaction with the Sun (ARTEMIS), which are equipped with modern particle and magnetic instruments. A main goal of lunar wake studies is to reveal the wake structure, i.e., distributions of plasma and electromagnetic properties in the wake, and its response to different solar wind and IMF conditions.

Solar wind plasma reentry into the wake can be understood in different regimes of plasma; studies in the early years emphasized its MHD aspects and have explained many large-scale observed features of the lunar wake. In the MHD regime, solar wind plasma is driven into the plasma void by the pressure gradient force [e.g., *Michel*, 1968; *Wolf*, 1968; *Spreiter et al*., 1970]. When plasma is sucked into the plasma void, the immediate consequence is the inward plasma flows all around the lunar wake, which transport plasma into the central wake and compress the magnetic field there. MHD theories predict a plasma and magnetic field depletion region surrounding the central lunar wake [e.g., *Whang and Ness*, 1970]. This region may expand at fast MHD wave velocities as a rarefaction front in the rest frame of the solar wind, forming a Mach cone surrounding the wake [e.g., *Johnson and Midgley*, 1968; *Michel*, 1968]. In the literatures, this depletion region is denoted as the "expansion region."

The lunar wake can be characterized well by plasma density, i.e., depletion of plasma. Initially, MHD simulations suggested that the plasma depletion region behind the Moon can extend along the solar wind to ~3–5 lunar radii ($R_M \sim 1738$ km) [*Spreiter et al*., 1970]; observations from the Wind satellite, however, turned out that the wake can extend to a much more distant downstream region of at least ~25 R_M [e.g., *Clack et al*., 2004], which is consistent with the results of a recent MHD simulation of *Xie et al*. [2013]. By using the decrease in the ion number density, *Zhang et al*. [2012] identified the lunar wake boundary and they found that the wake expands at fast MHD wave velocities in the plane perpendicular to the solar wind velocity, which confirmed the MHD prediction [e.g., *Johnson and Midgley*, 1968; *Michel*, 1968].

Plasma temperature is one of important plasma parameter related to plasma reentry behaviors. Observations from the Lunar Prospector satellite show that in the near-Moon region (~200 km above the lunar surface) the electron temperature increases by factors of ~4–10 [*Halekas et al*., 2005]. The increase in electron temperature was also observed farther downstream at 6.5 R_M by the Wind satellite [*Ogilvie et al*., 1996]. The ion temperature, however, has been observed to remain fairly constant [*Ogilvie et al*., 1996] while to be highly anisotropic in the downstream region [*Clack et al*., 2004]. The highly anisotropic ion temperatures are thought to be able to be interpreted by the double adiabatic theory [*Clack et al*., 2004]. In the theoretical models or simulations, however, in order to simplify calculations, plasma is generally assumed to obey the adiabatic law, $P\rho^{-\gamma} = \text{const}$ [e.g., *Wiehle et al*., 2011; *Wang et al*., 2011]. Consequently, when the density drops significantly in the wake, the temperature, if defined as P/ρ, is expected to decrease, too, but this is not consistent with observations. When a more general energy conservation function was used in an MHD simulation, plasma temperature can increase significantly by 3–4 orders [*Xie et al*., 2013]. They interpreted the increase in temperature as a consequence of adiabatic compression of refilling plasma flows encountering each other in the wake.

Magnetic perturbations associated with plasma refilling, e.g., field magnitude increase in the central wake and decrease in the expansion region were reported first by *Ness et al*. [1967]. The magnitude of the perturbations was observed to vary in response to changes in the solar wind ion β, the temperature, the angle between solar wind velocity and IMF, and the distance to the Moon [*Whang*, 1968a, 1968b, 1970]. Using data from Explorer 34 and 35, *Ogilvie and Ness* [1969] found that solar wind ion β is more important than other parameters in determining the magnitude of these perturbations. Intuitively and qualitatively, the magnetic perturbations are thought to be the consequence of compression and depression of inward flowing plasma, and quantitatively, they have been interpreted to be produced by diamagnetic currents arising from a pressure gradient on the wake boundary [*Ness et al*., 1968]. Electric currents corresponding to these field perturbations may be complicated. *Owen et al*. [1996] treated the Moon itself as a part of the plasma void and illustrated that the diamagnetic currents close on the dayside of the Moon for an IMF perpendicular to the solar wind. *Fatemi et al*. [2013], however, showed that the current system is much more complicated and strongly depends on the IMF directions. Another current induced by magnetic flux pileup may also flow through the dayside of the Moon if the Moon has finite conductivity [*Vernisse et al*., 2013]. Associated with the field magnitude disturbances, the field line geometries are also changed. As a result of plasma refilling, the field lines can bend toward the central wake in the plane perpendicular to the solar wind [e.g., *Russell*, 1993; *Khurana et al*., 2008]. *Wang et al*. [2011] proposed that if there is the finite conductivity of the Moon, field lines may bend toward the Moon. According to their MHD simulations, *Xie et al*. [2013], however, proposed that the pressure gradient in the solar wind velocity direction may prevent plasma flowing away from the wake and bend field lines toward the Moon (if the IMF is not purely parallel to the background solar wind velocity).

Large-scale structure of the lunar wake can be explained by MHD theories; however, many fine structures on subglobal scales in the wake require kinetic plasma theories, which in part derive from the relatively small spatial scale of the Moon ($R_M \sim 1738$ km) compared with the solar wind ion gyroradius of ~ 100 km [e.g., *Halekas et al*., 2011]. In the kinetic regime of plasma, although particle is often thought to refill into the wake driven by density gradient along field lines, a secondary effect, the ambipolar electric field, can also play a critical role in modifying the ion and electron behaviors. If driven only by the density gradient, the refilling of electrons is typically much faster than the ions owing to the large ion to electron mass ratio. In this case, plasma would no longer be quasi-neutral, and an electric field will set up which is commonly referred to as the "ambipolar electric field." In turn, this electric field will retard the electrons, accelerate the ions, and finally make them move together into the wake at velocities related to acoustic wave and make the plasma to be quasi-neutral. Meanwhile, a rarefaction front may propagate along field lines at acoustic wave velocities backward into the ambient solar wind and reduce density there. The ambipolar diffusion theory was introduced to the lunar wake studies by *Samir et al*. [1983].

Kinetic models have provided insight into many detailed wake features. Although the abovementioned model proposed by *Samir et al*. [1983] is simply 1-D, the ambipolar electric field in their model has been confirmed and measured systematically by the Lunar Prospector data [*Halekas et al*., 2005]. In this model, the ions can be accelerated along magnetic field lines from opposite sides of the wake and finally encounter each other in the wake forming counter-streaming ion beams, which have been observed by the Wind satellite beyond 6.5 lunar radii [*Ogilvie et al*., 1996; *Clack et al*., 2004] and have been represented well in 2-D kinetic simulations [e.g., *Nakagawa*, 2013]. If field lines are oblique to the background solar wind, the acceleration along field lines can increase the plasma bulk velocity on one side of the wake while decrease it on the opposite side [*Ogilvie et al*., 1996]. The broadband electrostatic noises associated with electrostatic instabilities excited by counter-streaming ion beams have been observed in the wake [*Kellogg et al*., 1996; *Bale et al*., 1997; *Farrell et al*., 1997] and have been successfully reproduced by 1-D particle-in-cell simulations [e.g., *Farrell et al*., 1998; *Birch and Chapman*, 2001] and 2-D particle-in-cell and hybrid simulations [e.g., *Birch and Chapman*, 2001; *Travnicek et al*., 2005]. The increase in electron temperature was found to increase in 1-D particle-in-cell simulations, although the ion temperature decreases [*Birch and Chapman*, 2001]. By using his 2-D particle-in-cell simulation, *Nakagawa* [2013] found, however, that the electron temperature remains nearly constant and that the ion temperature decreases just behind the Moon but increases in the more downstream wake where ions from both sides of the wake encounter. These 1-D or 2-D simulations suffer their dimensional limitations and obviously fail to capture some aspects of the response. For example, the disturbance of magnetic field cannot be described self-consistently with particles, and the magnetic field is generally assumed to be constant in these models [e.g., *Samir et al*., 1983; *Birch and Chapman*, 2001].

It would be desirable to obtain a full three-dimensional kinetic description of the lunar wake, while the resources needed for such calculations are prohibitive. In order to reduce the calculation expense while retaining some of the kinetic properties, 3-D models have been commonly carried out by using hybrid simulations instead of fully kinetic simulations. In 3-D hybrid simulations, electrons are treated as a massless fluid and the electron temperature is generally assumed to be constant [e.g., *Kallio*, 2005]. Ion temperature is seldom presented by 3-D hybrid simulations, while the anisotropy of ion distributions observed by [*Clack et al*., 2004] has been reproduced successfully by *Kallio* [2005]. *Fatemi et al*. [2012], however, proposed that the ion anisotropy at low altitudes in the wake can be caused by the lunar surface plasma absorption and solar wind temperature anisotropies.

In 3-D hybrid simulations, plasma refills the wake not only along the field lines but also perpendicular to the field lines [e.g., *Kallio*, 2005; *Roussos et al*., 2008; *Wiehle et al*., 2011; *Holmstrom et al*., 2012]. Plasma can be decelerated on one side of the plane determined by the IMF and the solar wind velocity while be accelerated on the other side [*Kallio*, 2005; *Roussos et al*., 2008], which asymmetry is different from that observed by *Ogilvie et al*. [1996] and needs to be confirmed by further observations. *Kallio* [2005] attributed this asymmetry to the ambipolar electric field $E = -(kT_e/e)\nabla \ln n$, which, in fact, is the electron pressure gradient term in the general Ohm's law if the electron temperature, T_e, is constant, while *Roussos et al*. [2008] attributed it to the Hall term of the generalized Ohm's law.

Not as the 1-D or 2-D kinetic simulations, magnetic field can be described self-consistent with particles in the 3-D hybrid simulations. The field enhancement in the central wake is always well reproduced by 3-D hybrid

simulations, and the distribution of the field depletion region surround the wake is found to depend on the IMF direction. When the IMF is parallel to the solar wind, the field depletion region will be all around the lunar wake [e.g., *Holmstrom et al*., 2012]. Magnetic field lines may bend toward the central wake if the IMF is not purely along the solar wind velocity direction [*Holmstrom et al*., 2012], which is consistent with predictions of, e.g., *Russell* [1993] and *Khurana et al*. [2008]. In the simulation of *Holmstrom et al*. [2012], the field lines are found to also bend slightly toward the Moon on one side of the wake and away from the Moon on the other side. When the electric field is described by the generalized Ohm's law but not only the ambipolar electric field, fine structures will develop in the electric field and the electric current [*Wang et al*., 2011; *Fatemi et al*., 2013; *Vernisse et al*., 2013].

Certainly, 3-D hybrid simulations can successfully reproduce plasma depletion region, the lunar wake, behind the Moon. The extension of the plasma depletion region along the solar wind may strongly depend on the IMF directions; for a given solar wind velocity, it is shortest when the IMF is perpendicular to the solar wind and longest if the IMF and the solar wind are parallel [*Holmstrom et al*., 2012]. It is found that the lunar wake expands all around the wake at the velocity of fast-mode MHD waves [*Wang et al*., 2011; *Wiehle et al*., 2011; *Holmstrom et al*., 2012; *Vernisse et al*., 2013], which is consistent with the MHD predictions [e.g., *Johnson and Midgley*, 1968; *Michel*, 1968; *Xie et al*., 2013]. *Roussos et al*. [2008] pointed out that when the background flow is submagnetosonic and sub-Alfvénic but supersonic, the wake can expand at ion acoustic velocity and basically along magnetic field lines, just as predicted by *Samir et al*. [1983].

Previously, the lunar wake was surveyed by single-spacecraft missions, such as the Lunar Prospector mission and the Wind satellite mission; only in the past 2 years have two spacecraft been simultaneously in orbit around the Moon. The two-spacecraft mission, the Acceleration, Reconnection, Turbulence and Electrodynamics of the Moon's Interaction with the Sun (ARTEMIS) mission, is an extension of the Time History of Events and Macroscale Interactions during Substorms (THEMIS) mission [*Angelopoulos*, 2011]. By design, when one ARTEMIS satellite crosses the lunar wake, the other is in the nearby solar wind, providing a unique opportunity to determine lunar wake properties linked to unambiguously known solar wind and IMF conditions, which is an advantage compared with previous missions [*Sibeck et al*., 2011]. The highly elliptic orbits of the ARTEMIS satellites allow wide survey of the plasma and electromagnetic environment in both the near-Moon region and in regions farther downstream (0 ~ 11 lunar radii). By using the data collected by the ARTEMIS spacecraft during their ~600 passes through the wake with well-determined solar wind and IMF conditions, we have characterized the plasma and field properties in the wake in three dimensions. In the next section, the instrumentation and the reconstruction methods are introduced; in section 3, all observations are presented, and our studies are discussed and summarized in the last two sections.

2. Instrumentation and Reconstruction Method

The ARTEMIS mission, the extension of the THEMIS mission, consists of two identical satellites, probes P1 and P2 [*Angelopoulos*, 2011]. By design, when one satellite crosses the lunar wake, the other is in the nearby solar wind, providing a unique opportunity to determine lunar wake properties for unambiguously known solar wind and IMF conditions [*Sibeck et al*., 2011]. The data analyzed in this paper were obtained from a three-dimensional velocity distribution plasma instrument, the electrostatic analyzer (ESA) [*McFadden et al*., 2008], and the fluxgate magnetometer (FGM) [*Auster et al*., 2008]. All the data are used at 3 s resolution which is the spin period of spacecraft.

Our quest to characterize the solar wind properties in the lunar wake is somewhat compromised by two factors. First, waves and discontinuities in the solar wind may not reach the two spacecraft simultaneously (even after accounting for propagation delay at the solar wind speed) because the phase fronts of such disturbances are often not aligned with the normal to the solar wind velocity vector. Thus, some data points acquired immediately following the arrival of a phase front at the upstream spacecraft may not be representative of the ambient solar wind conditions at the spacecraft in the lunar wake and should be excised from the observations. Such phase front timing mismatches between the two spacecraft will introduce a small degree of scatter into the differences of density and velocity. Second, in the low plasma density lunar wake, data from the ESA instrument may be contaminated by background counts from penetrating cosmic rays, which normally modify the differential flux counts very slightly. To some extent, this problem is eliminated by our use of calibrated data from the ARTEMIS archives, which have been corrected for

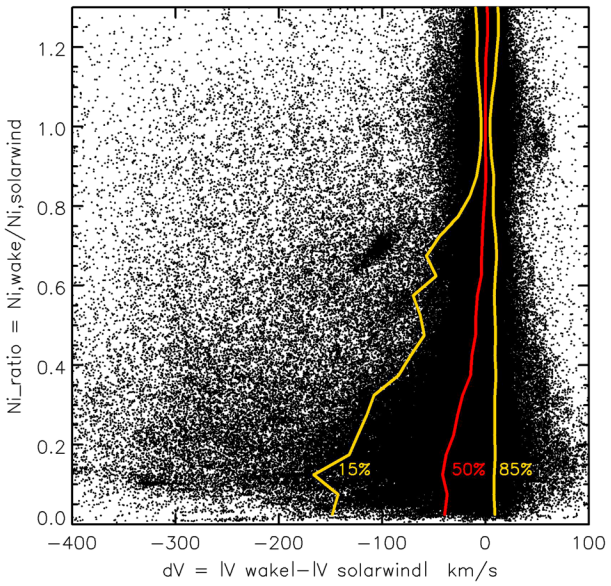

Figure 1. Normalized ion number densities, N_{i_ratio} plotted as a function of plasma flow perturbations dV. The normalized ion number densities are the ratios of the ion number densities in the wake to those simultaneously observed in the upstream solar wind, $N_{i\_ratio} = N_{i,wake}/N_{i,solarwind}$, and the perturbations of the solar wind velocity are defined by $dV = |V_{X,wake}| - |V_{X,solarwind}|$ (plasma is decelerated in the wake when $dV < 0$ and accelerated when $dV > 0$). Yellow and red curves mark the 15, 50, and 85 percentiles of dV for a given N_{i_ratio}, respectively. To further exclude possible contamination discussed in the text, only data between the 15 and 85 percentiles (between two yellow curves) are used in this paper.

nominal cosmic ray contamination. However, when the density in the lunar wake is extremely low, some of the measurements may be unreliable even after calibration. The reason is that measurements triggered by cosmic rays in the wake are likely to be highly anisotropic because of the effect of the Moon in blocking the arrival of counts from the upstream direction. This type of anisotropy produces a plasma distribution that appears to flow, possibly at high speed, antiparallel to the solar wind, suggesting that we view with skepticism such data.

In order to avoid including data contaminated by one or the other of these potential problems, we remove suspect values from our analysis in two ways. First, we discard all the wake data points with ion number density less than 0.1 cm^{-3}. Next, we use a procedure designed to remove data contaminated either by the phase front mismatches or the spurious effects of cosmic rays in the wake. We plot (see Figure 1) the normalized ion number densities as a function of the perturbation of the plasma velocity in the wake. The normalized ion number densities are the ratios of the ion number densities to those simultaneously observed in the upstream solar wind, $N_{i\_ratio} = N_{i,wake}/N_{i,solarwind}$, and the plasma velocity perturbation is defined as $dV = |V_{wake}| - |V_{solarwind}|$ (plasma is decelerated in the wake when $dV < 0$ and accelerated when $dV > 0$). The yellow and red curves mark the 15, 50, and 85 percentiles of values of dV corresponding to a given $N_{i,ratio}$. Data points that lie below the fifteenth percentile are widely, almost randomly distributed and are discarded. Data points above the 85th percentile are more compact, reflecting the fact that solar wind discontinuities introduce relatively small changes in the plasma parameters, but they are also discarded. Within the 15%–85% curves, the measurements appear to remain well organized even at densities approaching the lower bound of 0.1 cm^{-3}. These are the data that are retained for further analysis.

To relate observations to the directions of the IMF and solar wind, a dynamic orthogonal coordinate system referred to as the lunar solar magnetic system (LSM) is introduced as shown in Figure 2. The origin of the system is set at the center of the Moon. The direction antiparallel to the instantaneous solar wind velocity is defined as the system's X direction. The coordinate frame is dynamic because the solar wind direction is not steady. If the angle $\theta_{IMF,X} = <$ IMF, $-V_{SW} >$ between the IMF (B_{IMF}), and X is smaller than 90° (as shown in Figure 2 in red), Y is taken along the direction of $B_{IMF} \times X$; if the angle $\theta_{IMF,X}$ is larger than 90° (as shown in Figure 2 in blue), Y is taken along the direction of $-B_{IMF} \times X$. Z completes the orthogonal set through $X \times Y$. In this way the IMF B_{IMF} is remained parallel to the XZ plane and always satisfies $B_X B_Z > 0$. When this coordinate system is used, data bias arising from IMF rotations and changes of the solar wind flow direction are excluded. In this paper, the region with $(Y^2 + Z^2)^{1/2} < 1\ R_M$ and $X < 0$ is referred to as the "solar wind shadow" region, which is distinct from the "sunlight shadow" region because the velocity of solar wind is not necessarily along the direction radially away from the Sun.

From 27 June 2011 to 3 June 2013, the two ARTEMIS probes, P1 and P2, were in equatorial, highly eccentric lunar orbits with perigees and apogees of ~100 km (0.06 R_M) and 19,000 km (11 R_M), respectively

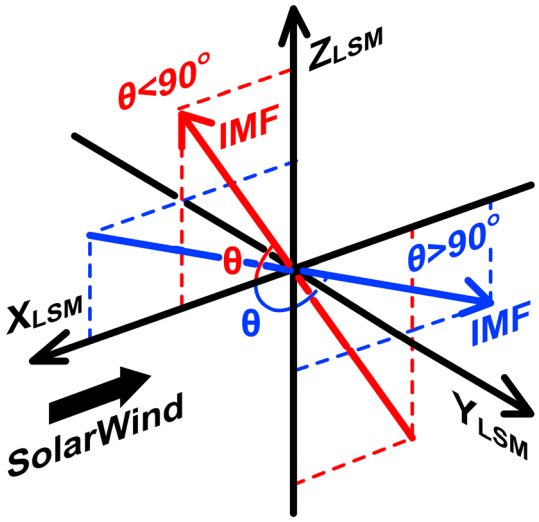

Figure 2. The dynamic orthogonal coordinate system referred to as the lunar solar magnetic system (LSM) used in this paper. The origin of the system is set at the center of the Moon. The system's X direction is always antiparallel to the instantaneous solar wind velocity. If the angle $\theta_{IMF,X}$ between the IMF (B_{IMF}) and X is smaller than 90° (as shown in red), Y is taken along the direction of $B_{IMF}\times X$; if the angle $\theta_{IMF,X}$ between B_{IMF} and X is larger than 90° (as shown in blue), Y is taken along the direction of $-B_{IMF}\times X\cdot Z$ completes the orthogonal set through $X\times Y$. In this way the IMF B_{IMF} is remained parallel to the XZ plane and satisfies $B_X B_Z > 0$.

[*Angelopoulos*, 2011]. They crossed the lunar wake ~600 times at a large range of X distances with passes well distributed in Y and Z. The wide spatial range of probe orbits allows us to reconstruct properties of the three-dimensional lunar wake by using plasma and field data collected during these orbits. In the direction perpendicular to the background solar wind velocity (Y and Z), the data point locations are expressed in terms of R_M (lunar radius = 1738.1 km). The length of the lunar wake along the X direction is sensitive to the solar wind speed (faster solar wind, longer lunar wake) [e.g., *Holmstrom et al*., 2012]. To correct for this source of variability, we normalized the X distance to the normal solar wind speed of 400 km/s. The equivalent X distance is equal to $400\cdot X/V_{SW}$, where V_{SW} is the instantaneous solar wind velocity. To establish the wake structure in the XY (XZ) plane, we display the distribution of the median values of the data in bins of $dX = 0.1\ R_M$, $dY = 0.1\ R_M$ over $Z = [-0.5, 0.5]\ R_M$ (in bins of $dX = 0.1\ R_M$, $dZ = 0.1\ R_M$ over $Y = [-0.5, 0.5]\ R_M$). The structures in the YZ plane are studied in three regions at different downstream ranges with the equivalent X distances equal to $[0, -3.5]\ R_M$ (Region I), $[-3.5, -7]\ R_M$ (Region II), and $[-7, -11]\ R_M$ (Region III), respectively. In each region, the bin size is $dY\times dZ = 0.1\ R_M \times 0.1\ R_M$.

The number of the plasma data points in each bin in the XZ, XY, and YZ planes is presented in Figure 3 in a logarithmic scale (the number of the magnetic field data points is larger than the plasma data points because we discarded possible contaminated plasma data in the lunar wake as described previously). We shall discuss the layout of Figure 3 in some detail because we use the same layout in most of subsequent figures when analyzing plasma and field properties of the lunar environment. Figures 3a and 3b show the distributions of the number of data of each bin in the XZ plane over $-0.5 < Y < 0.5\ R_M$ (Figure 3a) and in the XY plane over $-0.5 < Z < 0.5\ R_M$ (Figure 3b), respectively. Figure 3c–3e show the number of data of each bin in the YZ plane for cuts across the wake summed over a range of X in Region I ($X = [0, -3.5]\ R_M$), Region II ($X = [-3.5, -7]\ R_M$), and Region III ($X = [-7, -11]\ R_M$), respectively. The color bar is shown in the top right. Beneath each of the Y-Z plots, the number of data in each bins along the Y (Z) axis over the range of X defined for the labeled regions is plotted in blue (red) as a function of Y (Z). From Figure 3, it is clear that observations in the near-Moon region are enough and the well-distributed data points allow us to carry out the statistics of plasma and field properties in the space we study.

3. Observations

3.1. Plasma Number Density

Most solar wind plasma incident on the Moon's dayside surface is absorbed. Consequently, the lunar wake is described as a plasma depletion region. The plasma number density is, therefore, useful for distinguishing between the lunar wake and the undisturbed solar wind. Figure 4 represents the measured values of the ion number density within and around the lunar wake. We used the same layout as Figure 3, and in each bin the median value of the normalized ion number density ($N_{i,\ wake}/N_{i,solarwind}$) is shown. Here the subscript "wake" refers to observations from the spacecraft which crosses the wake (either in the wake or close to it), and the subscript "solarwind" refers to background solar wind observations obtained from the spacecraft which is in the nearby solar wind. When both of the spacecraft are located in the undisturbed solar wind, the

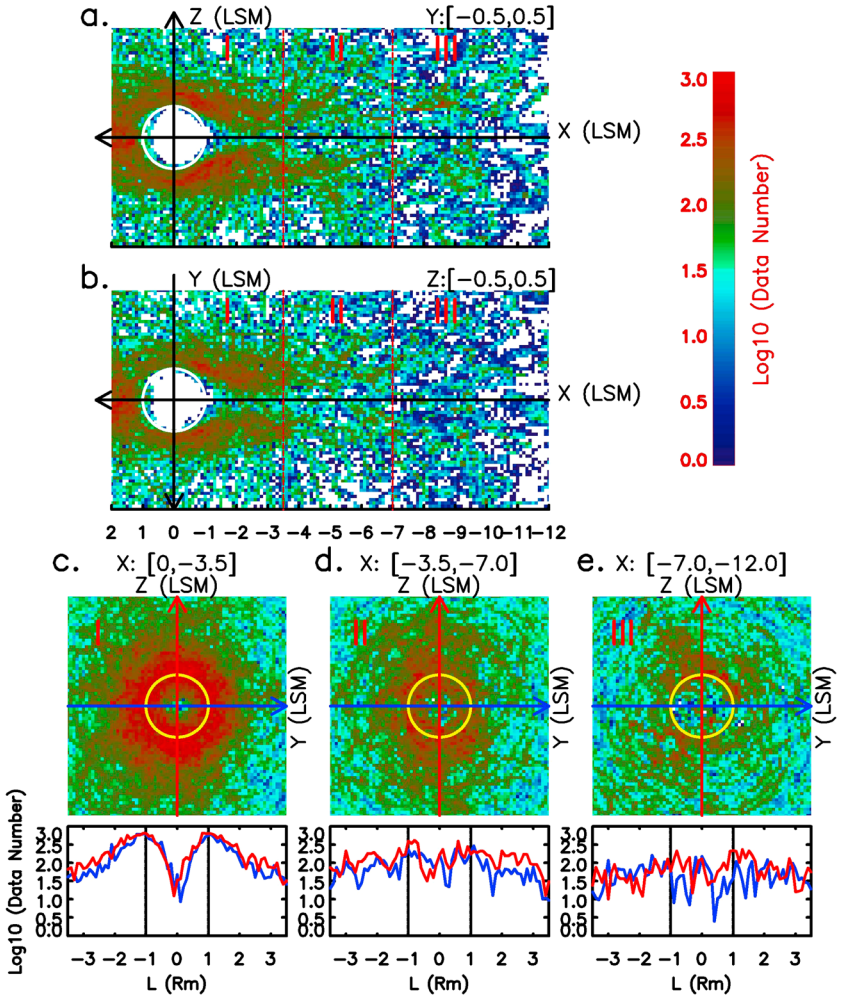

Figure 3. Distributions of the number of plasma data points in each bin defined in the text. (a) The *XZ* distribution of data point numbers summed over $-0.5 < Y < 0.5\ R_M$ with bin size of $dX \times dZ = 0.1\ R_M \times 0.1\ R_M$. (b) The *XY* distribution of data point numbers summed over $-0.5 < Z < 0.5\ R_M$ with bin size of $dX \times dY = 0.1\ R_M \times 0.1\ R_M$. (c–e) Top: the distributions in the *Y-Z* plane of data point numbers summed over *X* in Regions I, II, and III with the bin size of $dY \times dZ = 0.1\ R_M \times 0.1\ R_M$. Bottom: the data number profiles along *Y* axis (blue) and *Z* axis (red) summed over Regions I, II, and III, respectively. The *X* ranges for Regions "I," "II," and "III" are $X = [0, -3.5]$, $[-3.5, -7.0]$, and $[-7.0, -11.0]\ R_M$, respectively. The yellow circles in Figures 3c–3e represent the solar wind shadow boundary projected onto the *YZ* plane. In Figures 3c–3e (bottom), the boundary of the solar wind shadow is indicated by black vertical lines.

ratio $N_{i,\ \mathrm{wake}}/N_{i,\mathrm{solarwind}}$ approaches unity. According to the color bar shown in the top right, blue corresponds to the undisturbed solar wind density for which $N_{i,\ \mathrm{wake}}/N_{i,\mathrm{solarwind}} \sim 1$; green, red, and black dominate the wake region where $N_{i,\ \mathrm{wake}}/N_{i,\mathrm{solarwind}} < 1$. Beneath each of the *Y-Z* plots, the normalized density along the *Y* (*Z*) axis averaged over the range of *X* defined for the labeled regions is plotted in blue (red) as a function of *Y* (*Z*). It is clear that the ion density depletion region colored green, red, and black in Figure 3 (the lunar wake) extends at least out to 12 R_M.

In the near-Moon Regions I and II, the ion depletion region expands in the *Y* and *Z* directions and is confined well within a Mach cone as denoted by the rarefaction wavefront in Figures 4a and 4b (the outer boundary of the green region, marked by red lines). By comparing Figures 4a and 4b, it is seen that this expansion is faster in the *Y* direction, perpendicular to the IMF, (Figure 4b) than in the *Z* direction, oblique to the IMF (Figure 4a), and the flaring angle is ~9.3° in the *XZ* plane and ~12.5° in the *XY* plane (marked by red lines in Figures 4a and 4b). The well-structured Mach cone is absent in the farther downstream Region III (Figures 4a, 4b, and 4e). It should be noticed that the Mach cone shown in Figure 4 is a statistical result, and for different solar wind and IMF conditions the locations of the rarefaction front vary as studied by *Zhang et al.* [2012].

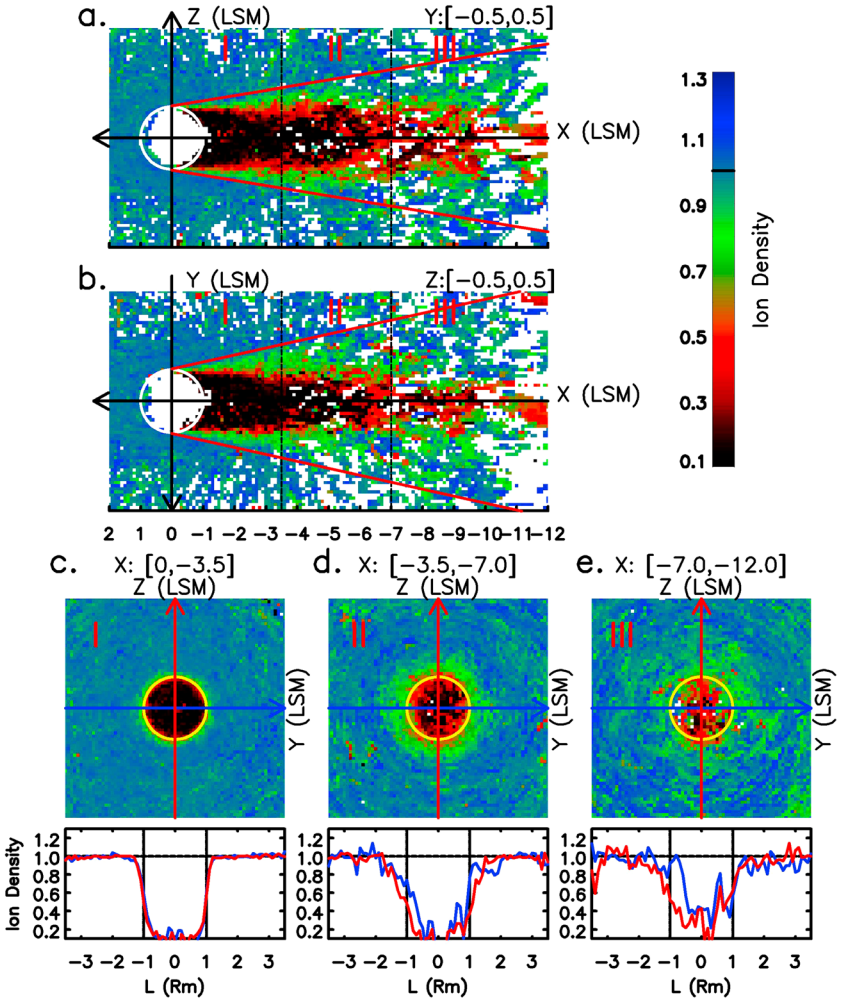

Figure 4. Distributions of the normalized ion number density ($N_{i,\mathrm{wake}}/N_{i,\mathrm{solarwind}}$). The median value of the ion number densities in each bin is shown, and the format and the bin sizes are the same as in Figure 3. (a and b) The red lines denote the wake boundary where density begins to decrease in these statistical plots.

The ion density inside the wake recovers as the downstream distance increases. Let us focus on the solar wind shadow region where $X < 0$ and $Y^2 + Z^2 < 1\ R_M$, identified by the yellow circles in the upper parts of Figures 4c–4e, and the black vertical lines in the lower parts of Figures 4c–4e. In the near-Moon Region I (Figure 4c), the normalized density drops abruptly to a level below 0.1 near the solar wind shadow boundary. As the downstream distance increases (e.g., Region II, Figure 4d), the ion density inside the central solar wind shadow recovers to a level above 0.1 and the density gradient on the solar wind shadow boundary becomes smaller. In the farther downstream region (Region III, Figure 4e), the density recovers to ~0.4 with a still smaller gradient. In the *XZ* or *XY* plane (Figures 4a or 4b), the dark-colored region behind the Moon, where $N_{i,\ \mathrm{wake}}/N_{i,\mathrm{solarwind}} < 0.2$, shrinks as the downstream distance increases and almost vanishes at *X* is ~ $-6.5\ R_M$. The shrink in the *Y* direction is faster than that in the *Z* direction (dark region in Figure 4b is narrower than that in Figure 4a), which makes the difference between the blue and red curves in the lower plots of Figures 4d and 4e.

The electron density has essentially the same properties as the ion density, and it is not shown here.

3.2. Plasma Temperature

Plasma temperature is useful for diagnosis of particle behaviors. Figure 5 shows the distributions of the logarithm of the normalized ion temperature, $\log(T_{i,\mathrm{wake}}/T_{i,\mathrm{solarwind}})$. Black represents the undisturbed solar wind temperature, and red, green, and blue represent higher temperatures ($\log(T_{i,\mathrm{wake}}/T_{i,\mathrm{solarwind}}) > 0$). The

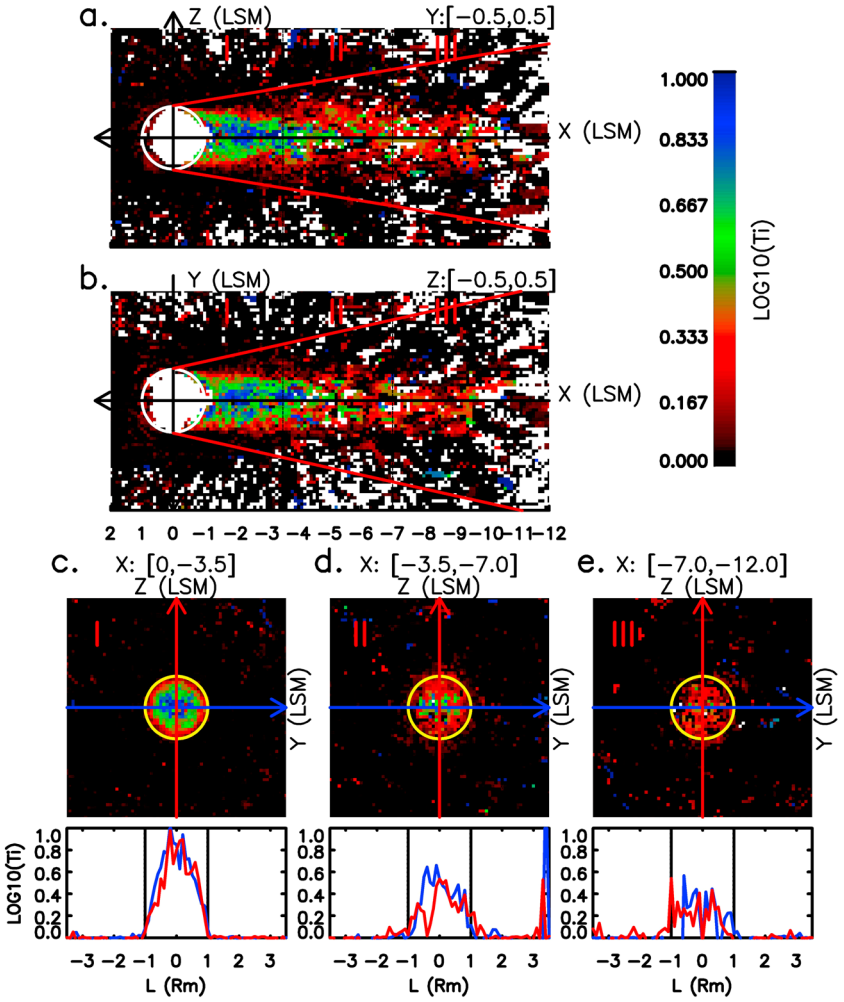

Figure 5. Distributions of the normalized ion temperature ($T_{i\ \mathrm{wake}}/T_{i,\mathrm{solarwind}}$) on a logarithmic scale. The format is the same as in Figure 3.

temperature increase region is basically confined within the solar wind shadow and shrinks as the downstream distance increase. The magnitude of the temperature increase is about 1 order of magnitude in the near-Moon region (Region I) and decreases as the downstream distance increases.

Figure 6 compares the parallel temperature ($\log(T_{i,\mathrm{para,wake}}/T_{i,\mathrm{solarwind}})$ in Figure 6a) and the perpendicular temperature ($\log(T_{i,\mathrm{perp,wake}}/T_{i,\mathrm{solarwind}})$ in Figure 6b) of the ion distribution in the *YZ* plane in the near-Moon region (Region I). Although both parallel and perpendicular temperatures increase significantly inside the solar wind shadow, the perpendicular temperature increasing region is broader particularly along the *Z* direction than the parallel temperature as evidently marked by the green color in Figures 6a and 6b.

The electron temperature distribution is shown in Figure 7. As the ion temperature, the electron temperature also increases within the solar wind shadow. In the near-Moon region (Region I, Figure 7c), it increases toward the central wake and peaks at the central wake, and the peaked electron temperature rises by ~0.8 order which is consistent with the Lunar Prospector observations [*Halekas et al.*, 2005]. In the distant wake, the peak temperature is lower and the region of elevated temperature is less structured (Region III, Figure 7e). By comparing Figure 7 with Figure 5, it is seen that the magnitude of electron temperature increasing is less than that of the ion temperature increasing in the near-Moon wake (for example, Region I in Figures 5c and 7c). No significant difference is found between the distributions of parallel and perpendicular electron temperatures (not shown).

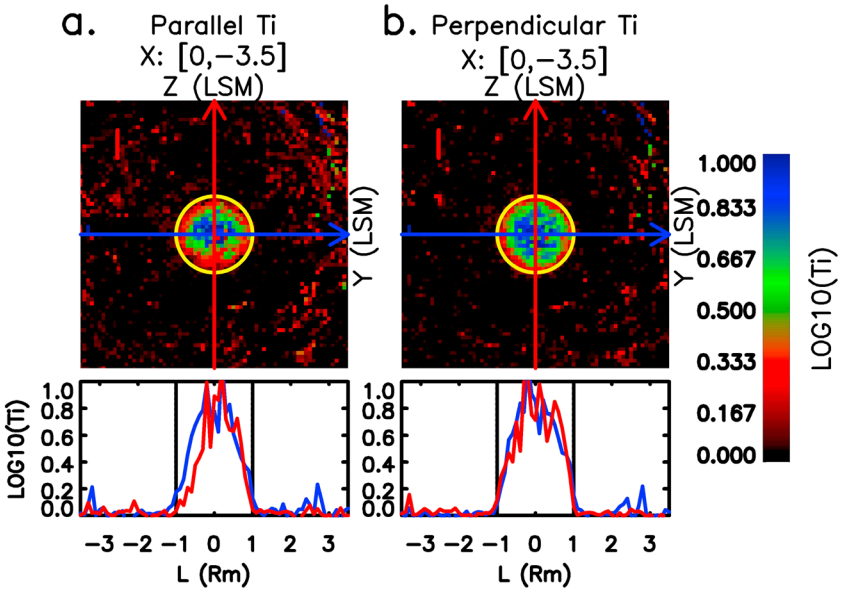

Figure 6. Comparison of the normalized parallel ($T_{i,\mathrm{para,wake}}/T_{i,\mathrm{solarwind}}$) and perpendicular temperature ($T_{i,\mathrm{perp,wake}}/T_{i,\mathrm{solarwind}}$) distributions in the *Y-Z* plane in Region I ($X = [0, -3.5]\ R_M$). The format is the same as in Figure 5c.

3.3. Pressure

In the lunar wake, the plasma density is extremely low and the temperature is high; what, then, is the pressure distribution in the wake region? Figure 8 shows the total thermal pressure (the sum of ion and electron thermal pressures, $P_{\mathrm{th}} = P_i + P_e$), observed by ARTEMIS within and around the lunar wake. Within the shadow region, the effect of the temperature increase does not compensate for the plasma density depletion due to absorption by the Moon, and a significant thermal pressure drop (black region) is clearly present within the solar wind shadow in the near-Moon region (Region I). The pressure drop extends farther downstream into Regions II and III, but the magnitude of the decrease is smaller than in the near-Moon region.

In the shadow region, the total pressure, defined as the sum of the thermal and magnetic pressures ($P_T = P_i + P_e + P_M$), changes far less than the thermal pressure (compare Figures 8 and 9). Figure 9 shows the total pressure distribution using the same color bar as adopted for Figure 8. A reduced total pressure region (red) is located mainly within the solar wind shadow and is present principally in the near-Moon region (Region I). The pressure gradient in the *Y-Z* plane is smaller in the distant wake than it is in the near-Moon region as evident from Figures 9c–9e. Enhancement of the field magnitude in the central wake does not seem to cancel out the thermal pressure depletion. In this case plasma is being accelerated toward the wake center as shown in the following sections.

3.4. Magnetic Field

Figure 10 shows the distributions of the normalized field magnitude around the lunar wake ($B_{\mathrm{wake}}/B_{\mathrm{solarwind}}$). Two distinct features, field magnitude increase and field magnitude reduction, are seen in the lunar wake.

The field magnitude enhancement region ($B_{\mathrm{wake}}/B_{\mathrm{solarwind}} > 1$) (shown in red and dark green in Figure 10) is located principally within the solar wind shadow. The magnitude of the field enhancement is a function of the distance to the Moon. The field increase region starts immediately behind the Moon, and the field magnitude continues to increase as the downstream distance increases (compare Figures 10c–10e).

In Figure 10, just outside the solar wind shadow lies a blue-colored region of reduced magnitude of the normalized field. This region is generally confined by the rarefaction wavefront in the Mach cone and, in literature, is referred to as the expansion region [*Ogilvie et al.*, 1996]. In our data, the weak-field region extends from the near-Moon region out to $X = -12\ R_M$, and as the downstream distance increases the weak field region grows increasingly large (Figures 10c–10e) and the magnitude of the field reduction increases (compare Figures 10c–10e). The reduction is particularly clear in some of the traces in the lower panels of

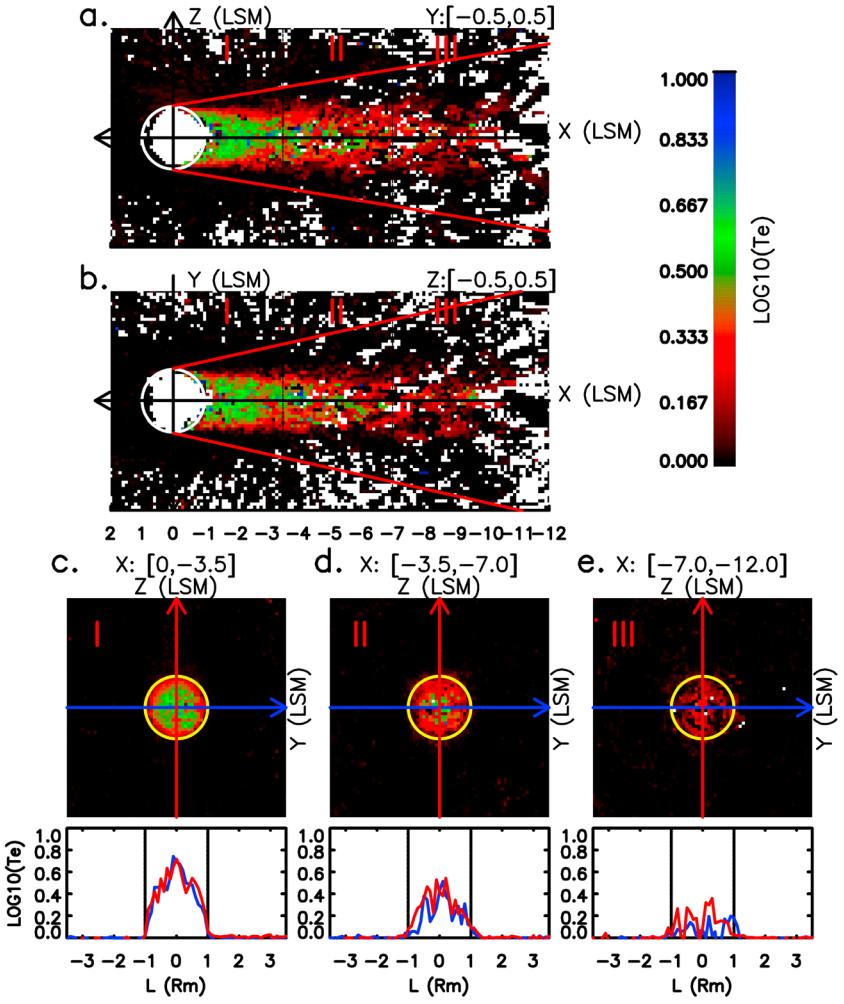

Figure 7. Same as in Figure 4 except for the electron temperature.

Figures 10c–10e. Comparison of the red and blue curves in those panels shows that the reduction is significant along the *Y* axis (blue curves) but very weak along the *Z* axis (red curves). This asymmetry about the *X* axis may be controlled by the angle $\theta_{IMF,X} = <\text{IMF}, -V_{SW}>$ between the IMF and $-V_{SW}$ (*X* axis). Figure 11 shows the subsets of data in Figures 10c and 10d with $\theta_{IMF,X} = [0,30]$ and [150,180] (quasi-parallel case) and $\theta_{IMF,X} = [60,120]$ (quasi-perpendicular case), respectively. In the quasi-parallel case (Figure 11a), blue dominates within the entire expansion region (outside and all around the solar wind shadow denoted by the yellow circle in Figure 11a), and both the red and blue curves dip within that region (outside the black vertical lines in the bottom part of Figure 11a). For the quasi-perpendicular case, however, field reduction occurs only in the expansion region near the *XY* plane (blue outside the yellow circle in Figure 11b), and the field increases slightly in the region near the *XZ* plane. The bottom part of Figure 11b also shows that the field reduction occurs only for the blue curve (on the *Y* axis in the top part), not for the red one (on the *Z* axis in the top part). Field reduction asymmetry appears for the quasi-perpendicular case but not for the quasi-parallel case, which is also observed by the Lunar Prospector in the near-Moon wake [*Halekas et al.*, 2005]. It should be pointed out that $\theta_{IMF,X}$ controls not only the magnitude of the field reduction in the expansion region but also the magnitude of the field enhancement in the central wake. It is evident in Figure 11 that the magnitudes of the field enhancement in the central wake are larger for the quasi-parallel case than for the quasi-perpendicular case, which is also clearly seen in the results of the 3-D hybrid simulation done by *Wang et al.* [2011].

The magnitude of the field perturbation depends not only on the downstream distance and the angle $\theta_{IMF,X} = <\text{IMF}, -V_{SW}>$ as we have shown but also on the solar wind ion beta, $\beta_{i,solar}$, defined as the ratio of the

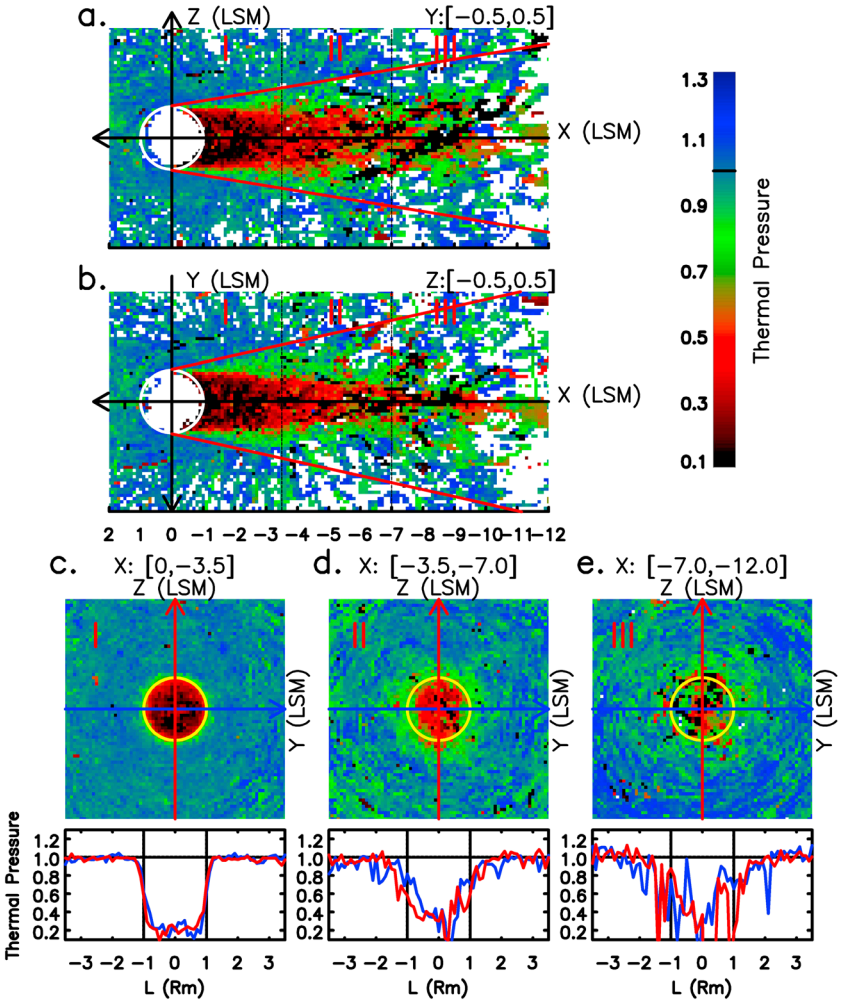

Figure 8. Same as in Figure 4 except for the thermal pressure, P_{th} ($P_i + P_e$).

solar wind ion pressure to the magnetic pressure. The field enhancement ratio ($\alpha = B_{wake}/B_{solarwind} - 1$) of all the data points in the near-Moon region with $0 > X > -2$ R_M in the lunar wake is plotted in Figure 12 as a function of solar wind ion beta $\beta_{i,solarwind}$ ($\beta_{i,solarwind}$ is plotted in a logarithmic scale). As shown in Figure 12 (bottom), the solar wind ion beta, $\beta_{i,solar}$, falls mainly in the range [0.2, 10]. Within this $\beta_{i,solar}$ range, all the data points are confined well by $\alpha = \pm 0.33\beta_{i,solarwind}$ (red and green curves in Figure 12 (top)). Since the probability of $\beta_{i,solarwind}$ is low beyond 4, we do not have enough data points to explore relation between $\beta_{i,solarwind}$ and α in the large beta region.

Lunar wake formation not only modifies the IMF magnitude but also bends the IMF within the wake. Figure 13 shows the distribution of IMF bend angles in the *YZ* plane of the LSM system for all data with $X = [-11, 0]$ R_M (Regions I–III). Here the bend angle is defined as the angle (whose tangent is B_Y/B_Z) between the *Z* axis and the projection of a magnetic field vector on the *YZ* plane. In different quadrants in *Y-Z* plane the dominant color near the solar wind shadow boundary changes. In those quadrants with $Y > 0$ and $Z > 0$ or $Y < 0$ and $Z < 0$, red dominates near the solar wind shadow boundary (yellow circle), indicating that most bend angles in these two regions are positive. In the diagonally opposite quadrants, however, blue dominates near the solar wind shadow boundary and the bend angles are basically negative. These observations indicate that the magnetic field lines inside the lunar wake are bent and that a magnetic flux tube that goes through the lunar wake (black lines) is pinched locally as shown by the yellow lines in Figure 13, which is consistent with the field magnitude increase in the wake.

We also explored the field line bending in the *XZ* plane. Figure 14 shows the distribution of IMF bend angles due to perturbations of the *X* and *Z* components of the magnetic field. Here the bend angle is defined as the

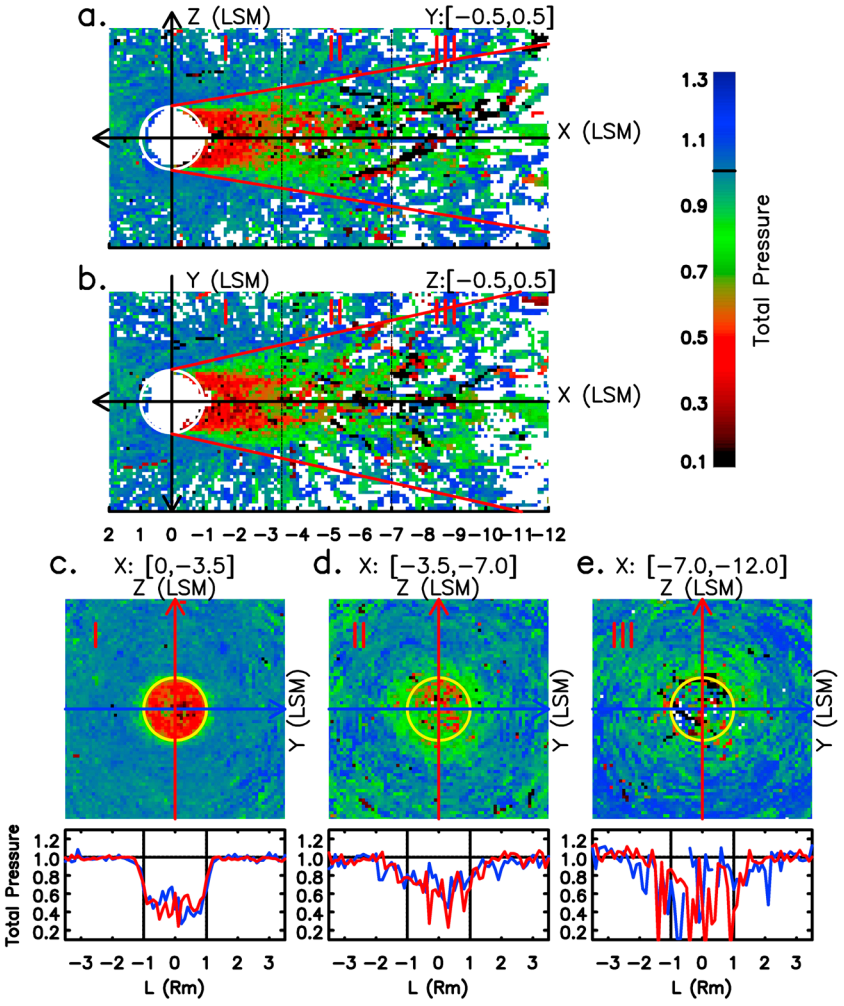

Figure 9. Same as in Figure 4 except for the total pressure, P_T ($P_i + P_e + P_M$).

angle between the perturbed field lines and the undisturbed IMF in the *XZ* plane (remember that the IMF does not necessarily point along the *Z* axis). The positive (negative) angle implies that the magnetic field line rotates anticlockwise (clockwise). It is evident in Figure 14 that in the wake where $Z > 0$ the bend angles are basically negative and in the region where $Z < 0$ the bend angles are positive, which indicates that the field lines behind the Moon bulge toward the Moon as schematically shown by the yellow curve in Figure 14a.

3.5. Plasma Flows

Plasma flow is another key parameter that helps to reveal the evolution of the lunar wake. We use V_{wake}-$V_{solarwind}$ to identify flow perturbations, where V_{wake} is the plasma velocity measured in the lunar wake and $V_{solarwind}$ is the corresponding undisturbed solar wind velocity. We will discuss flow perturbations in the *YZ* plane and along the *X* axis separately.

First, let us focus on the flow perturbations in the *Y* and *Z* components. Figure 15 shows the distributions of these flow perturbations in the *YZ* plane in Regions I, II, and III, respectively. Vectors in Figure 15 mark the direction of flow perturbations, and colors indicate the magnitude of the *Y-Z* flow perturbation. Inside the central lunar wake in Region I, the flow perturbations are basically along the *Z* direction toward the central region; in the outer wake in Region I (but still inside the solar wind shadow boundary), however, the flow perturbations point basically radially inward and the magnitude of these flow perturbations (purple arrows) is weaker than in the central wake region (red and green arrows) (Figure 15a). Outside the lunar wake in Region I, the directions of the disturbed flows are disordered, and the magnitude is small (mostly light purple). In Region II, the disturbed flows

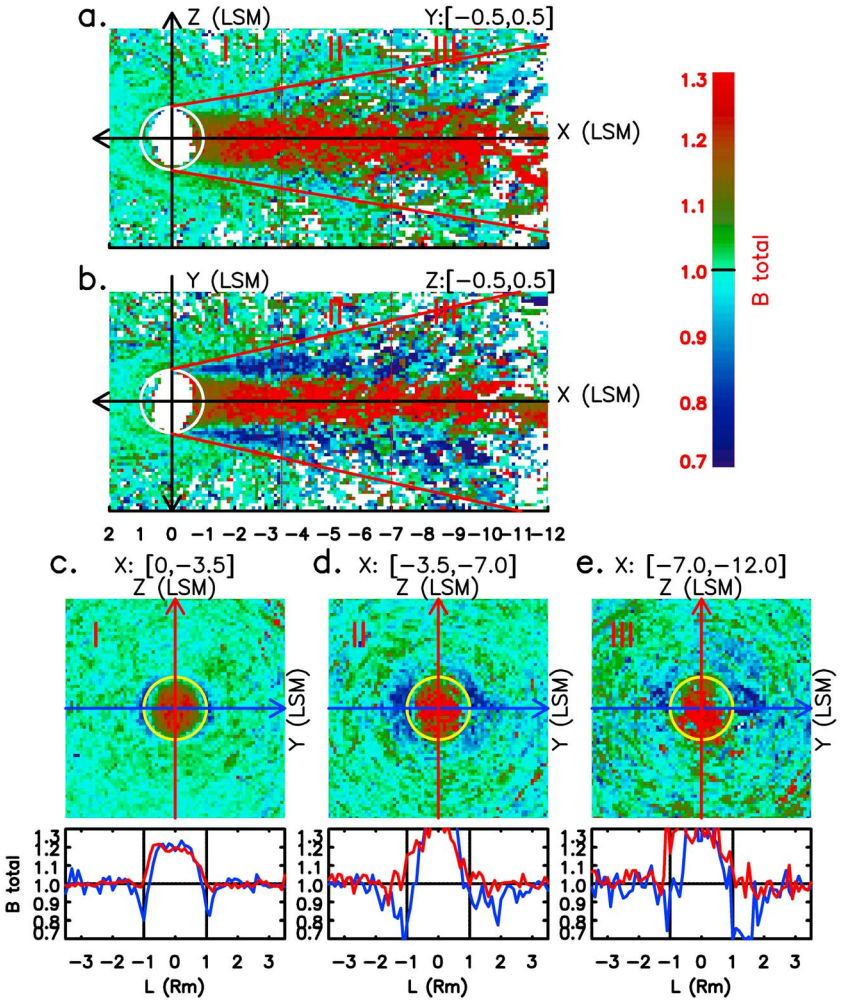

Figure 10. Same as in Figure 4 except for the normalized field magnitude, B_T ($B_{wake}/B_{solarwind}$).

are present in an expanded region confined within the Mach cone (compare Figures 15a and 15b). In the central wake in Region II, these perturbations are disordered a little, while in the outer region of the lunar wake the disturbed flows point radially inward (outside the solar wind shadow in Figure 15b). Flow perturbations in Region III are basically inward in the wake but are less structured than in regions closer to the Moon (Figure 15c).

Figure 16 shows the distributions of the magnitude of the *X* component of the plasma flow perturbations ($dV_x = |V_{x,wake}| - |V_{x,solarwind}|$) in the *XZ* plane (Figure 16a), the *XY* planes (Figure 16b), and in the *YZ* planes in Regions I–III (Figures 16c–16e). Cyan and green indicate that the perturbation is small; blue represents negative values ($|V_{x,wake}| - |V_{x,solarwind}| < 0$), implying deceleration of plasma; red corresponds to positive values ($|V_{X,wake}| - |V_{X,solarwind}| > 0$), implying acceleration of plasma. It is seen that plasma is decelerated significantly by ~150 km/s in the central wake in the near-Moon region. Farther down the wake, the deceleration is less than in the near-Moon region. Flow deceleration appears to be asymmetric in the *XZ* plane in this region, and the blue region mainly occurs in the region with $Z < 0$ in the *XZ* plane (Figure 16a), while in the region where $Z > 0$ and $X < -1.5\ R_M$, the blue region is small and plasma continues to flow at velocities close to the solar wind velocity. Not any clear asymmetry is seen in this region in the *XY* plane (Figure 16b). Beyond $X = 3.5\ R_M$, the plasma deceleration is seen but not well structured.

4. Discussion

The key questions on the wake formation are how plasmas refill into the wake and how these plasmas modify the magnetic field in the wake. Plasma and magnetic properties associated with refilling are thus critical to

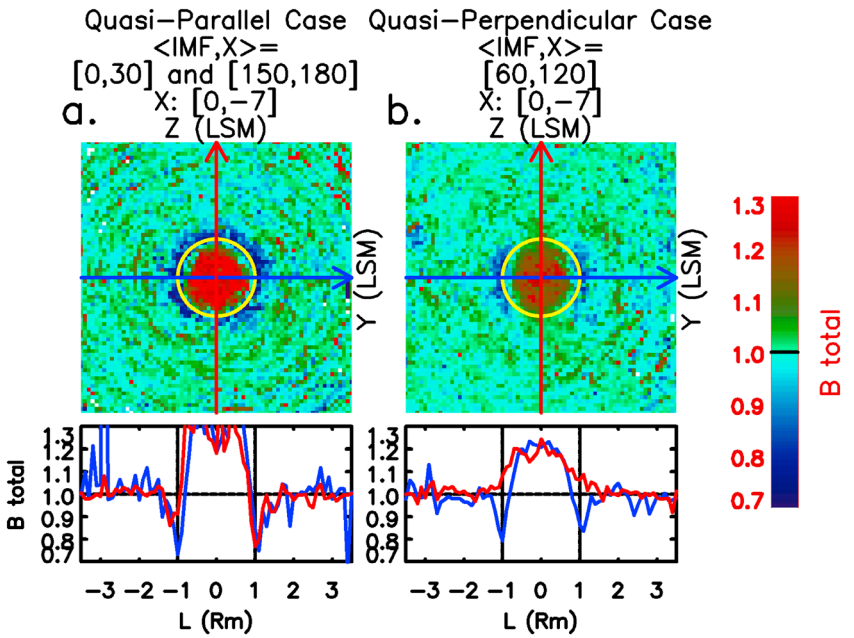

Figure 11. (a) Distributions of the normalized field magnitudes in Regions I and II for the quasi-parallel case with the angle between the IMF and the *X* axis equal to [0, 30] or [150, 180]° and (b) the quasi-perpendicular case with the angle equal to [60, 120]°. The formats are the same as Figure 10c.

answer these questions and can give insight into the lunar wake formation. By using the ARTEMIS data, we have depicted the wake by plasma number density, temperature, pressure, flow, and magnetic field in a 3-D way. Although our statistical approach has undoubtedly smoothed out some small-scale features, to first order, our results provide a good global picture of the lunar wake for comparison with simulations. In the literatures, many theories or models have been established to understand the lunar wake formation. These models implement different level of approximation to deal with plasma in the lunar wake. Our data suggest that some wake features can be described sufficiently by MHD theories, whereas some other features require more precise descriptions by the two-fluid, hybrid, and even fully kinetic descriptions.

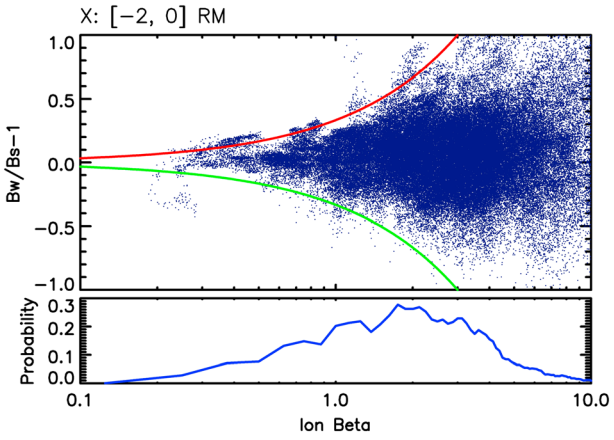

Figure 12. (top) A scatterplot of the field enhancement rates ($\alpha = B_{wake}/B_{solarwind} - 1$) of all the data points with $0 > X > -2\ R_M$ in the near-Moon wake as a function of solar wind ion beta, $\beta_{i,solar}$, defined as the ratio of the solar wind ion pressure to the magnetic pressure. In the low beta range [0, 4], all the data points are confined within $\alpha = 0.33\beta_{i,solarwind}$ and $\alpha = -0.33\beta_{i,solarwind}$. (bottom) The probability of $\beta_{i,solar}$ distributions.

4.1. Wake Length

By using the distribution of ion number density, the global wake can be depicted clearly as shown in Figure 4. The very low density region with density less than 0.2 (the black region in Figures 4a and 4b) in our data extends to about 6–7 R_M downstream of the Moon, which is consistent with the results of recent simulations (e.g., hybrid simulation of *Wang et al.* [2011] and MHD simulation of *Xie et al.* [2013]). The density recovers toward the background level of the ambient solar wind as the downstream distance increase, and it is seen that the lunar wake can extend at least out to 12 R_M downstream from the Moon. *Clack et al.* [2004] have shown that the wake can extend to 25 R_M downstream. In the hybrid simulation of *Holmstrom et al.* [2012], the wake length was found to strongly depend

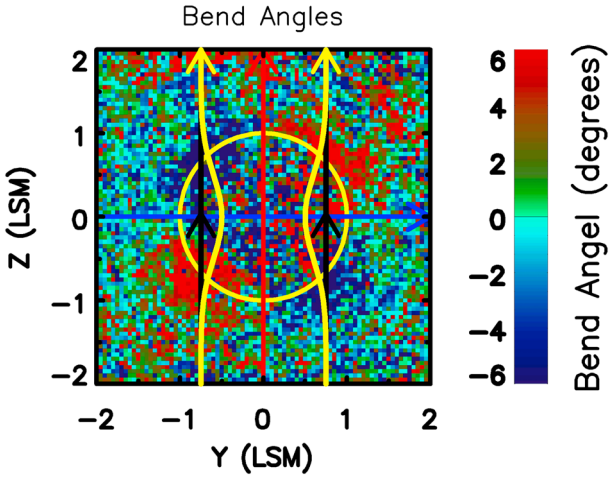

Figure 13. Distribution in the *YZ* plane of the bend of the *Y* and *Z* components of the field. The positive (negative) angle implies that the magnetic field line bends clockwise (anticlockwise) in the *Y-Z* plane. The black vertical lines show the undisturbed IMF flux tube, and the yellow curves schematically show the bent field lines and the locally pinched flux tube.

on the angle between the solar wind velocity and the IMF, $\theta_{IMF,X} = <$ IMF, $-V_{SW}>$. We checked the wake length for the quasi-perpendicular ($\theta_{IMF,X}$ ~90°) and quasi-parallel ($\theta_{IMF,X}$ ~0° or 180°) cases, respectively; it is shown that, however, this dependence is not evident as well as shown by the MHD simulation of *Xie et al*. [2013].

4.2. Wake Expansion

When plasma refills the wake, the wake expands backward into the ambient solar wind as a rarefaction wavefront. MHD theories predicted that the expansion is at velocities of fast-mode waves [e.g., *Johnson and Midgley*, 1968; *Michel*, 1968]. The expansion thus should be anisotropic, and it is faster in the direction perpendicular to the magnetic field than in the direction oblique to the magnetic field [e.g., *Xie et al*., 2013]. Although the rarefaction wake front was predicted to propagate at ion acoustic wave velocity along field lines in the simple 1-D ambipolar diffusion model [*Samir et al*., 1983], results of many 3-D kinetic models, however, show the fast MHD expansion [e.g., *Wang et al*., 2011; *Wiehle et al*., 2011; *Holmstrom et al*., 2012; *Vernisse et al*., 2013]. *Roussos et al*. [2008] suggested that the expansion velocities may depend on the background flow. When the background flow is submagnetosonic and sub-Alfvénic but supersonic, the rarefaction wavefront can move outward at ion acoustic velocity and basically along magnetic field lines; otherwise, the front may expand at fast MHD velocities. By using the ARTEMIS data, *Zhang et al*. [2012] studied 160 wake crossing events and found that the wake boundaries are located near the fast wavefronts.

In this study, however, the lunar wake expansion has been shown intuitively in Figures 4a and 4b on the basis of the number density data of over 600 wake crossing events collected by the ARTEMIS mission. In the *XY* plane (Figure 4b), the rarefaction wavefront expands in the direction perpendicular to the IMF, whereas in the *XZ* plane (Figure 4a) the expansion is oblique to the IMF. By comparing Figures 4a and 4b, the anisotropy of wake expansion is clearly seen, and the rarefaction front moves faster in the direction perpendicular to the IMF than oblique to the IMF (the flaring angle in the *XY* plane is about 12.5° (Figure 4b) and is about 9.3° in the *XZ* plane (Figure 4a)), which is consistent with the MHD theories [e.g., *Johnson and Midgley*, 1968; *Michel*, 1968]. In our data, the averaged solar wind number density, temperature, and IMF magnitude are 3.6 cm^{-3}, 30 eV, and 5 nT, respectively, which give the fast-mode MHD velocity of ~89 km/s in the direction perpendicular to the magnetic field. By using the flaring angle $\theta_F = 12.5°$ in the *XY* plane and the normalized solar wind velocity $V_{SW} = 400$ km/s, we estimated the expansion velocity $V = V_{SW}\tan(\theta_F)$ to be ~89 km/s in the *XY* plane, which is almost identical to the fast-mode wave velocity. In the *XZ* plane, the wake expansion may be oblique to the IMF, and in this case, the fast-mode wave velocity depends on the angle between the solar wind and the IMF $\theta_{IMF,X} = <$ IMF, $-V_{SW}>$. If we assume $\theta_{IMF,X} = 90°$, in the *XZ* plane the fast-mode wave will propagate along the IMF and the fast-mode velocity can be estimated to be 69 km/s. By using the 9.3° flaring angle in the *XZ* plane, the rarefaction wavefront is estimated to expand at a velocity of ~66 km/s, which is also very close to the fast MHD wave velocity in this direction.

Besides the outward propagating fast MHD front discussed above, there may be a front propagating inward toward the central wake. Let us focus on the dark regions in Figures 4a and 4b, in which the normalized density is less than 0.2. As the downstream distance increases, the dark region shrinks and finally almost disappears beyond ~6.5 R_M, particularly in the *Y* direction (perpendicular to field lines) (Figure 4b); in the *Z* direction (in the *XZ* plane in Figure 4a), however, the dark region shrinks more slowly than in the *Y* direction, which is also shown in the lower panel of Figure 4d in which the blue curve is narrower than the red curve. When the 0.2 density front propagates inward to the central wake in the rest frame of the solar wind, it leads

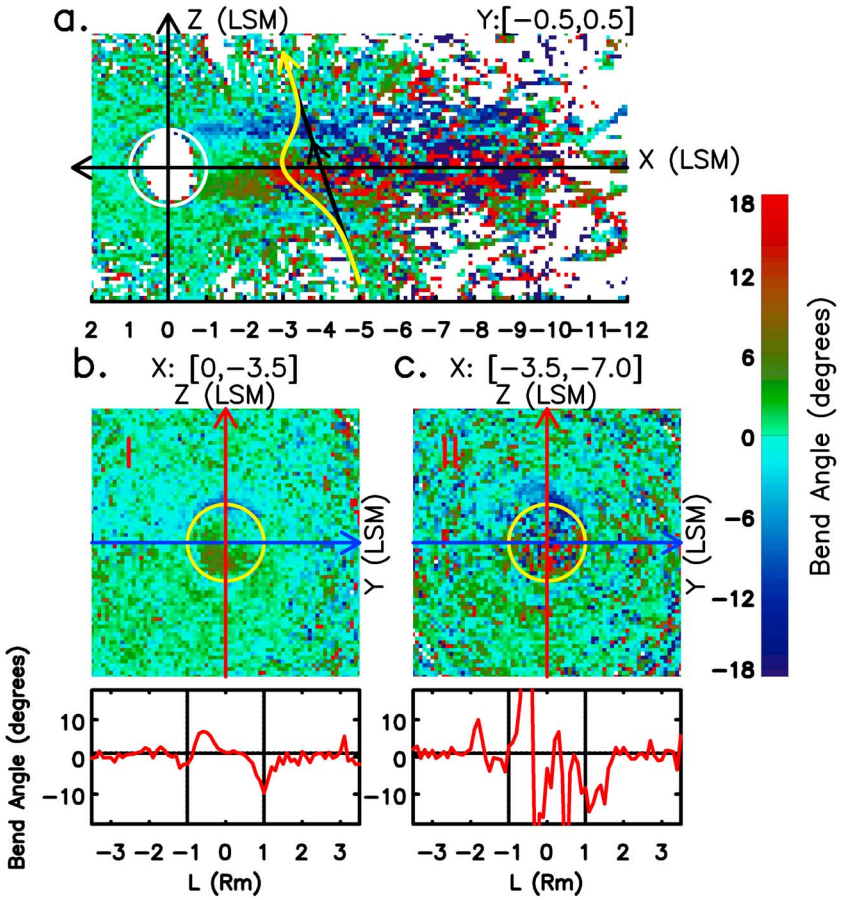

Figure 14. (a) Distribution in the *XZ* plane of the bend of the *X* and *Z* components of the magnetic field. The positive (negative) angle implies that the magnetic field line bends anticlockwise (clockwise) in the *X-Z* plane. The black line schematically shows an undisturbed IMF field line oriented in a nominal direction selected only for illustrative purpose, and the yellow curve schematically shows a bent field line. After passing through the Moon, the field lines bulge toward the Moon. (b) Distribution of the field line bend in the *Y-Z* plane in Region I ($X = [0, -3.5]\ R_M$). (c) Distribution of the field line bend in the *Y-Z* plane in Region II ($X = [-3.5, -7.0]\ R_M$).

to increases in both the field magnitude and the thermal pressure relative to their previous (upstream) values. The asymmetry of the propagation and the in-phase perturbations in plasma and magnetic field are consistent with fast MHD wave properties. By using the fact that the dark region disappears beyond 6.5 R_M in the *XZ* plane, we estimate the averaged inward propagating velocity of the 0.2 density front as roughly 62 km/s in the direction perpendicular to the IMF, which is, however, much smaller than the fast-mode MHD wave.

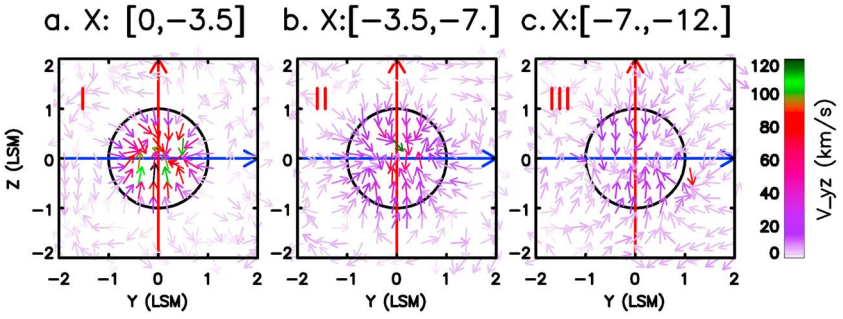

Figure 15. Distributions in the *Y-Z* plane of flow perturbations in the *Y* and *Z* components, defined as V_{wake}-$V_{solarwind}$, in Region I, II, and III, respectively. Flow vectors mark the flow directions, and colors represent the magnitude of the *YZ* flow perturbation.

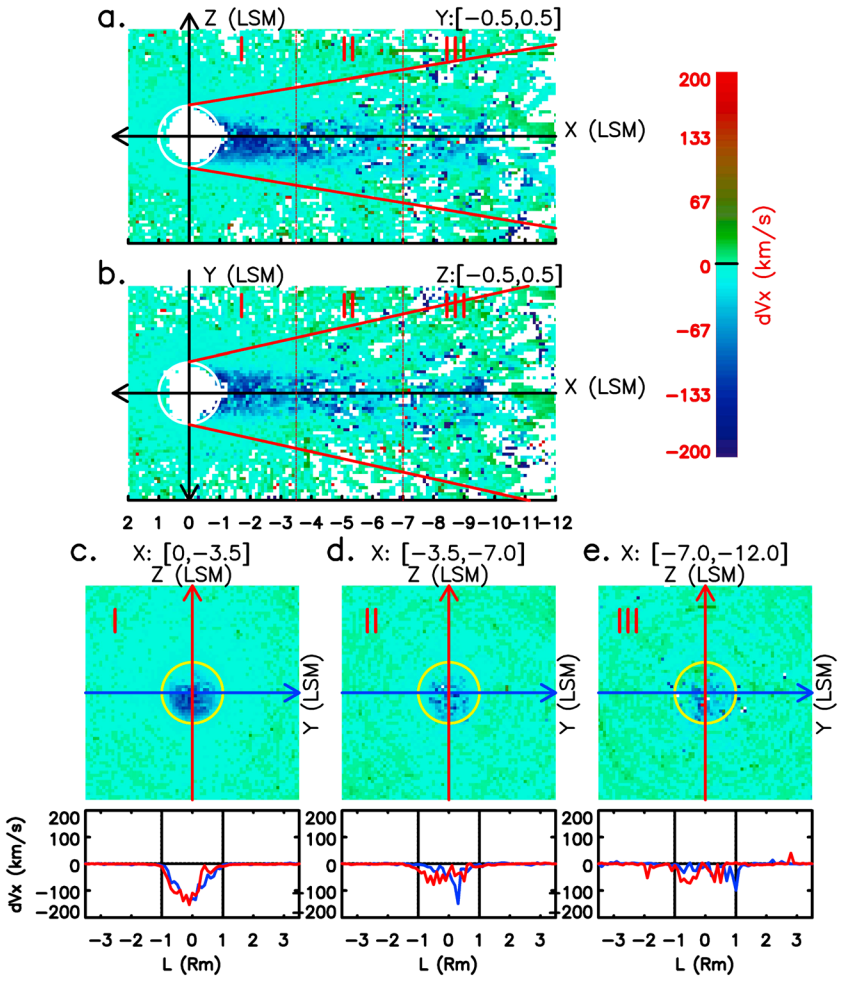

Figure 16. Distributions of flow perturbations in the *X* component, $dV_x = |V_{wake}| - |V_{solarwind}|$, in the (a) *XZ* plane, (b) *XY* plane, and in *YZ* plane for (c) Region I, (d) Region II, and (e) Region III, respectively.

Notice that this velocity is an averaged propagating velocity since, when the front propagates inward in the rest frame of the solar wind, the plasma and magnetic properties change significantly. In addition, the wave in the wake may have the acoustic wave properties [e.g., *Samir et al*., 1983], and we calculate the acoustic wave velocity to be 63 km/s, which is comparable to the propagation velocity of the 0.2 density front in the direction perpendicular to the IMF. The properties of the inward moving front need more observational and theoretical analyses.

4.3. Plasma Refilling

The data analyzed in this work clarify how plasma refills the depleted region in the wake, and most of our observations show that plasma refilling can be understood within the MHD regime. The total pressure (Figure 9, the sum of the thermal pressure and magnetic pressure) drops significantly behind the Moon. The subsequent total pressure gradient force thus accelerates the ambient solar wind plasma all around the wake into the plasma void (Figure 15). The perpendicular component of the inward flow compresses the magnetic field locally leading to the field magnitude enhancement (Figure 10) and the bend of field lines in the *YZ* plane (Figure 13) [*Russell*, 1993; *Khurana et al*., 2008]. This compression continues from just behind the Moon to $X = -12\ R_M$, and meanwhile, it is seen that the field magnitude continues to increase from the near-Moon region to that distant wake (Figure 10). This compression accounts for a field enhancement that is a function of the downstream distance as suggested theoretically by *Whang et al*. [1968a, 1968b]. The field magnitude in the wake region must become the same as in the background solar wind somewhere farther downstream; however, that distance must be beyond the scope we studied ($2 > X > -12\ R_M$).

Some observations associated with plasma refilling, however, cannot be described by MHD theories, and more precise models are needed. When plasma refills into the wake, the velocity component in the *X* direction (solar wind direction) is significantly decelerated as shown in blue in Figures 16a and 16b. We will discuss the flow deceleration in the near-Moon wake region ($0 > X > -1.5\ R_M$) later, and now let us focus on the range of $-1.5\ R_M < -7\ R_M$ in the *XZ* plane (Figure 16a). It is noticed that the flow perturbations are asymmetrically distributed around the *X* axis in the *XZ* plane and that plasma is decelerated mainly where $Z < 0$ and is less changed or decelerated where $Z > 0$. In the LSM coordinate system we used, field lines always satisfy $B_X B_Z > 0$. For this magnetic field configuration, according to *Ogilvie et al*. [1996], however, solar wind plasma is predicted to be accelerated along field lines on both sides of the wake, producing a positive V_X perturbation in the $Z > 0$ region and a negative V_X perturbation in the $Z < 0$ region, whereas whose magnitudes should be the same in both sides ($Z > 0$ and $Z < 0$). Thus, the asymmetrically distributed flow perturbations in the *XZ* plane indicate additional flow deceleration in the wake, which obscures flow accelerations for $Z > 0$.

In addition, the asymmetry of the flow perturbations in *Vx* about the *X* axis in the *XY* plane proposed by *Kallio* [2005] and *Roussos et al*. [2008] is not seen in our data (Figure 16).

Since plasma refilling occurs mainly along the "field-aligned" direction, it is expected that particles from opposite sides of wake will form counter-streaming beams somewhere downstream in the wake [e.g., *Kallio*, 2005; *Nakagawa*, 2013]. Counter-streaming ion beams have been observed at 6.5 R_M downstream of the Moon by the Wind satellite [*Ogilvie et al*., 1996; *Clack et al*., 2004]. Electrostatic instabilities arising from counter-streaming ion beams can excite broadband electrostatic noise [*Kellogg et al*., 1996; *Bale et al*., 1997; *Farrell et al*., 1997, 1998; *Birch and Chapman*, 2001]. Direct observations of the counter-streaming particles and the broadband electrostatic noises are not given in our study; our data, however, give some evidences of them. It is shown that the very low density region (density less than 0.2, dark region in Figure 4) disappears beyond $6 \sim 7\ R_M$, suggesting that plasmas from opposite sides encounter each other and fully mix. Meanwhile, beyond 7 R_M (Region III), distributions of many parameters, such as ion density, temperature, pressures, and magnetic field, are not well structured as they are in the near-Moon region (Regions I and II) and they may be scattered by waves or poorly determined when there are counter-streaming beams in the distribution function.

In addition, the ion density has almost the same distribution as the electron (not shown) in our data, which indicates electrons refill the wake together with ions. This result is consistent with the MHD description as well as some kinetic descriptions [e.g., *Samir et al*., 1983]. In a 2-D particle-in-cell simulation, *Nakagawa* [2013], however, found that the negative electric charge on the nightside of the Moon can cause significant difference between the ion and electron density in the near-Moon wake. This difference is not seen in our data.

4.4. Ion and Electron Temperature

Our data show that both ion and electron temperatures increase abruptly by almost 1 order just behind the Moon (Figures 5 and 7). Temperature is determined as the averaged kinetic energy of particles in the plasma bulk velocity frame, and energy dispersion effect and wave scattering can account for these increases in temperatures. The higher-energy particles in the ambient solar wind move more rapidly than do the lower energy particles along the magnetic field lines into the wake, and thus, in the near-Moon region, the central wake is filled mainly by higher-energy particles and additional waves may be needed to randomize these particles thereby elevating the temperature (as shown by the energy spectra in the wake). As the downstream distance increases more and more lower energy particles move into the wake and the temperature decreases gradually. A comparison of the ion and electron temperatures in the near-Moon region (Region I in Figures 5 and 7) shows that the ion temperature increases more rapidly than the electron temperature along a line from the wake boundary to the central wake and that the electron temperature recovers to the background level more rapidly than does the ion temperature (the high ion temperature region extends farther down the wake than does the electron temperature). The difference between the two contributions can be understood in terms of the difference of mass. At a fixed temperature, electron velocities are greater than ion velocities by the square root of the mass ratio. The faster thermal velocities of electrons enable even the lowest-energy electrons to reach the center of the wake very rapidly, maintaining a

relatively low temperature distribution throughout the wake. The presence of ambipolar electric field must have modified the electron temperature in the wake [*Halekas et al*., 2005]; however, we cannot extract this effect from our statistical data.

Our qualitative interpretation of the ion and electron temperature variation through the wake has not been tested by simulations. The 3-D MHD simulation of *Xie et al*. [2013] produced increased plasma temperature in the wake, while the difference between the ion and electron temperatures indicates that the temperatures must be treated in a kinetic way. To simply assume electron or ion to be "isothermal" [e.g., *Kallio*, 2005] or "adiabatic" [e.g., *Wiehle et al*., 2011; *Wang et al*., 2011] seems not a proper way since these assumptions are not consistent with our observations. The increase in electron temperature has been successfully reproduced in 1-D particle-in-cell simulation [*Birch and Chapman*, 2001], while the ion temperature decreases in this simulation. *Nakagawa* [2013] found that the ion temperature starts to increase beyond the downstream distance of 2 R_M in the wake, and it is attributed to an effect of counter-streaming ions.

Ion temperature anisotropy is observed in our data (Figure 6), and the perpendicular temperature increasing region (green in Figure 6b) is evidently broader than that of the parallel temperature (green in Figure 6a), particularly along the *Z* directions, suggesting that perpendicular temperature increases more rapidly than the parallel temperature. An extreme large anisotropy in the ion temperature has been observed by the Wind satellite, which has been interpreted by a double adiabatic theory [*Clack et al*., 2004]; however, this model calls for the perpendicular temperature to increase slightly while the parallel temperature drops significantly. The latter is expected because, in the double adiabatic model, the parallel temperature is proportional to n_i^2/B^2 and the ion number density drops significantly in the wake. This prediction differs from what is observed in our data. According to their hybrid simulation, *Fatemi et al*. [2012] proposed that the anisotropy of ion temperature at low altitudes in the wake can derive from the effects of lunar surface plasma absorption and solar wind temperature anisotropies. In our data, however, an alternative explanation related to the magnetic perturbations in the wake may account for the observations. As shown in Figure 10, the magnetic field increases by about 1.2–1.3 times in the wake, forming a mirror structure (Figure 13); this mirror magnetic field may contribute to the anisotropy of ion temperature. The discrepancy between observations and models may hint that neither the adiabatic nor the isothermal assumption is appropriate for the wake. Three-dimensional fully kinetic simulations are required to understand the ion and electron refilling behavior.

4.5. Field Magnitude Perturbations

In addition to the downstream distance (Figure 10), the solar wind ion beta $\beta_{i,\mathrm{solarwind}}$ (Figure 12) and the angle $\theta_{\mathrm{IMF},X} = <$ IMF, $-V_{\mathrm{SW}} >$ (Figure 11) also control the magnitude of the field enhancement. We used diamagnetic currents to interpret these controls [*Ness et al*., 1968]. Figure 17 shows a schematic of particle trajectories and field lines for a perpendicular case in which the IMF is perpendicular to the solar wind velocity. The typical solar wind ions gyrate with a gyroradius of $r_i = a_1 \cdot T_{i,\mathrm{perp}}{}^{1/2}/B_{\mathrm{SW}}$, where $T_{i,\mathrm{perp}}$ is the perpendicular ion temperature, B_{SW} is the IMF field strength, and a_1 is a constant coefficient. When the solar wind passes the lunar terminator, particles whose guiding centers are more than 1 gyroradius r_i above the surface remain unaffected independent of their gyrophases. Representative ion trajectories with a particular gyrophase are plotted in blue on both sides of the Moon in Figure 17a. In Figure 17a, red dotted lines delimit the region in which all particles, independent of gyrophase, are absorbed by the Moon. This situation applies to those particles with guiding centers more than 1 gryoradius below the lunar surface at the terminator and includes, for example, particles on trajectories plotted in red in Figure 17a. For particles whose guiding centers are at a distance equal to or less than 1 gryoradius either above or below lunar surface at the terminator (between the blue and the red dotted lines), absorption depends on gyrophase. For example, particles moving along the black trajectory marked "1" in Figure 17a are absorbed by the lunar surface, whereas those moving along the black trajectory marked "2" in Figure 17a pass around the Moon. Thus, a sharp density gradient with spatial scale of about 2 r_i develops at the terminator and in the near-Moon wake, and the ion diamagnetic current layers (marked by green arrows in Figure 17a) whose thickness, *L*, can be related to the ion gyroradius, $L = a_2 \cdot r_i$. Here to be simple, only the ion response is considered; if electrons are involved, the condition will be complicated and the thickness and the magnitude of the current will be modified. The current density inside this current layer *j* depends on the solar wind ion number density n_i and the perpendicular thermal velocity proportional to $T_{i,\mathrm{perp}}{}^{1/2}$, i.e., $j = a_3 \cdot n_i \cdot T_{i,\mathrm{perp}}{}^{1/2}$. The total current inside the current layers thus is of order $I = j \cdot L = (a_3 \cdot n_i \cdot T_{i,\mathrm{perp}}{}^{1/2}) \cdot (a_2 \cdot a_1 \cdot T_{i,\mathrm{perp}}{}^{1/2}/\mathrm{B_{SW}}) = a_1 \cdot a_2 \cdot a_3 \cdot n_i \cdot T_{i,\mathrm{perp}}/\mathrm{B_{SW}}$.

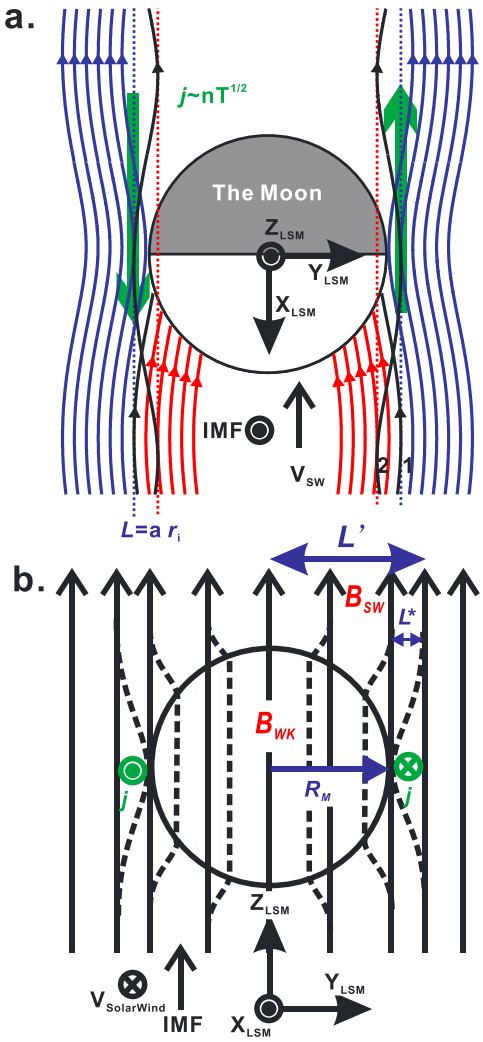

Figure 17. The particle trajectories, diamagnetic current system and field configurations in the near-Moon region for the quasi-perpendicular case. (a) Representative ion trajectories in the near-Moon region viewed in the *XY* plane (IMF is outward and solar wind is upward). The trajectories of ions whose gyrocenters are more than 1 gyroradius away from the terminator (outside the blue dotted lines) are shown in blue. The motion of these particles is not affected by the presence of the Moon. The trajectories of particles whose gyrocenters are more than 1 gyroradius below the lunar surface at the terminator (between the two red dotted lines) are shown in red. All these particles hit the dayside lunar surface and are absorbed by the Moon. The trajectories of ions whose gyrocenters are less than 1 gyroradius to the lunar surface at the terminator are shown in black. These particles may or may not be absorbed by the Moon depending on their gyrophases. The ions with black trajectories labeled as "1" are absorbed, whereas the ions labeled as "2" go around the terminator and pass through. A sharp gyrocenter gradient thus establishes and leads to a diamagnetic current system at the terminator and in the near-Moon wake (marked by green arrows). (b) Field configurations in the near-Moon region viewed in the *YZ* plane. The dashed lines represent bent field lines and the solid lines represent the undisturbed IMF. The diamagnetic currents lead to the abrupt field increase and bend in the near-Moon region.

The magnitude of the field perturbations, $\Delta B = B_{wake}\text{-}B_{solarwind}$, is related to the magnitude of the total current by $\Delta B = a_4 \cdot I$, according to which we obtain $B_{wake}/B_{solarwind} - 1 = b \cdot (kn_i T_{i,perp})/(B_{SW}^2/2\mu_0)$, where b is a combined coefficient of a_1, a_2, a_3, a_4, the Boltzmann constant k and the permeability of free space μ_0. The right side of this equation is proportional to the solar wind ion beta $\beta_{i,solar}$, and the left side is the rate of field perturbation ($\alpha = B_{wake}/B_{solarwind} - 1$) as shown in Figure 12. Thus, $\alpha = b \cdot \beta_{i,solar}$. Our data in Figure 12 show that in the near-Moon region ($X > -2\ R_M$) the magnitudes of field perturbations are confined by $\alpha = \pm 0.33\beta_{i,solar}$ when $\beta_{i,solar} < 3$. The perturbations scatter between $\alpha = \pm 0.33\beta_{i,solar}$ because of effects of data point locations or the corresponding IMF conditions ($\theta_{IMF,X}$).

In fact, when the IMF is parallel to the solar wind (parallel case), a ring-like diamagnetic current forms all around the lunar terminator, instead of being confined near the *XY* plane as in the perpendicular case in Figure 17. As shown in Figure 11, the ring-like diamagnetic current in the parallel case makes stronger field perturbations than does the more confined diamagnetic current near the *XY* plane that develops in the perpendicular case. This result is consistent with recent hybrid simulations [e.g., *Wang et al.*, 2011]. Thus, the angle between the solar wind and the IMF also controls the magnitude of the field perturbations.

The diamagnetic current is ring like in the terminator region for the parallel case; in the perpendicular case, however, it is unclear how these diamagnetic currents close. *Owen et al.* [1996] proposed that these currents close through the diamagnetic currents on the dayside of the Moon for the case when IMF is perpendicular to the solar wind, and *Fatemi et al.* [2013] proposed that for a more general case (IMF is oblique to the solar wind), part of the diamagnetic currents close through the current at the Mach cone boundary. *Vernisse et al.* [2013], however, proposed that if the Moon has finite conductivity, part of the current may also close through the dayside while this current is associated with field pileup on the dayside of the Moon. In our data, however, the magnetic perturbations associated with these possible currents on the dayside are not well distinguished from the magnetic perturbations possibly due to the surface magnetic anomalies or the low spatial resolution of our statistics (0.1 R_M).

Thus, by the diamagnetic current, field perturbations are initiated at the lunar terminators ($X \sim 0\ R_M$), for example, as shown in Figure 17b. That is why the field magnitude increases to about 1.1 right behind the Moon ($X \sim -1\ R_M$) (Figure 10). This instant field magnitude enhances right behind the Moon is consistent with previous observations from the Lunar Prospector [e.g., *Halekas et al*., 2005]. They are also well represented in some 3-D hybrid simulations [e.g., *Wang et al*., 2011; *Fatemi et al*., 2013], but sometimes they are not so evident [e.g., *Holmstrom et al*., 2012]. After passing the terminator, pressure gradient force continues to compress the wake and makes continuous increase in field magnitude in the farther distant lunar wake. Certainly, our discussion on the diamagnetic current is incomplete; in particular, we did not consider the response of electrons.

4.6. Field Line Bends and Plasma Deceleration

Figure 13 shows that the magnetic field lines bend in the *YZ* plane to form a mirror structure, which we have interpreted as a consequence of the inward flow compression. In the *XZ* plane, the magnetic field lines are found to bulge toward the Moon as shown in Figure 14a: in the region with $Z > 0$ the field lines rotate clockwise in the *XZ* plane, while when $Z < 0$ they rotate anticlockwise. This type of bend can be seen even in the farther distant wake (Regions II), but it is better structured in the near-Moon region (Regions I). In the hybrid simulation of *Holmstrom et al*. [2012], field lines are found to bend toward or away from the Moon. In the 3-D hybrid simulation of *Wang et al*. [2011], it was found that finite conductivity of the Moon can produce field line bending. However, if the field bending is caused by the finite conductivity of the Moon, plasma deceleration and field line bending should have been observed in the upstream region, but it was not (see Figures 14 and 16). In the 3-D MHD simulation for the case of IMF not parallel to the background solar wind velocity, *Xie et al*. [2013] find bends in the field in the same sense as in the data and also a pressure gradient in the solar wind velocity direction. However, the plasma flow in their simulated wake is accelerated and thus not consistent with our data.

According to our data, flow deceleration does occur in the wake. It is of interest to interpret this result, and we offer two possible interpretations. One possible mechanism would attribute deceleration just behind the Moon to a positive pressure gradient along the solar wind flow direction maintained by the wake plasma refilling process, and just such a pressure gradient is seen in Figure 8 (as also in the simulation of *Xie et al*. [2013]). As discussed earlier, very close to the Moon, the supermagnetosonic solar wind is unable to fill the void region through plasma flow along the field direction. Farther down the tail, however, the solar wind is able to reach the center of the wake and it is this refilling that sets up the pressure gradient in the *X* direction. The deceleration, largest near the center of the wake (Figure 16), bends the field (Figure 14); the net force in the *X* direction includes the pressure gradient force and the opposing magnetic curvature force.

We can speculate on an alternate explanation. There is evidence to show that the Moon is surrounded by a tenuous atmosphere of charged dust particles [.e.g., *Rennilson and Criswell*, 1974]. The charged dust is present on both dayside and nightside of the Moon at altitudes up to 100 km above the lunar surface [e.g., *Stubbs et al*., 2006]. On the dayside, the newly picked-up dust particles will be swept back onto the surface of the Moon. However, heavy charged dust grains behind the Moon may be picked up by the convective electric field of the solar wind. Due to their large masses, these dust grains, densest close to the Moon, can locally slow down the solar wind plasma and thus bend the field lines.

5. Summary

By using simultaneous measurements of the unperturbed solar wind and IMF properties to characterize upstream condition accurately at high temporal resolution, we have been able to reconstruct the plasma and field structure of the three-dimensional lunar wake and to establish many features of the wake that rely on knowledge of the IMF and solar wind conditions. We have shown how the key plasma and field parameters, the ion and electron density, temperatures, thermal pressure, magnetic pressure (field magnitude), total pressure, and field and flow perturbations, vary through the wake.

Wake disturbances are present immediately behind the Moon, driven by diamagnetic currents at the lunar terminator and extend at least out to the downstream distance of 12 R_M. In the rest frame of the solar wind, the lunar wake expands outward as a rarefaction wave at fast MHD mode velocities; another wavefront forms inside the lunar wake and propagates inward. This inward propagating wavefront can also be a fast MHD

wave but needs to be confirmed by more analyses. Beyond about 6.5 R_M downstream of the Moon, plasma parameters are not well structured probably because plasma from two sides of the wake mixes together and leads to instabilities which scatter those parameter structures. Plasma is accelerated into the wake through either ambipolar electric fields or pressure gradient forces. Plasma moving inward perpendicular to the background field compresses the magnetic field and leads to continuous increase of magnetic field in the wake. The increase of temperature for both ions and electrons is a consequence of an energy dispersion effect that develops when plasma refills the wake, a process that can be understood thoroughly through fully kinetic analysis. The magnitude of the field perturbation is found to depend both on the downstream distance and on the solar wind ion beta and the angle between the solar wind velocity and the IMF. After passing the Moon, the IMF is found to bulge toward the Moon, which is unexpected and may be caused by a plasma pressure gradient force or/and the pickup of heavy charged dust grains behind the Moon.

Acknowledgments

This work was supported by the National Science Foundation of China (41274171), the specialized research fund for Chinese State Key Laboratories under project Y22612A33S, the Chinese Academy of Sciences project (KZZD-EW-01-3), the Scientific and Technological Innovation and Cooperation Group of Chinese Academy of Sciences, and the Hundred Talent Program of Chinese Academy of Sciences. Work at UCLA was supported by NASA through THEMIS 443869-TM-22620 and THEMIS/ARTEMIS project NAS5-02099. We also specially acknowledge with appreciation J. McFadden for use of ESA and K.H. Glassmeier, U. Auster, and W. Baumjohann for the use of FGM data provided under the lead of the Technical University of Braunschweig and with financial support through the German Ministry for Economy and Technology and the German Center for Aviation and Space (DLR) under contract 50 OC 0302. We would also like to thank Xuzhi Zhou and Jasper Halekas for valuable discussions.

Yuming Wang thanks Tomoko Nakagawa and an anonymous reviewer for their assistance in evaluating this paper.

References

Angelopoulos, V. (2011), The ARTEMIS mission, *Space Sci. Rev.*, *165*, 1–23, doi:10.1007/s11214-010-9687-2.

Auster, H. U., et al. (2008), The THEMIS fluxgate magnetometer, *Space Sci. Rev.*, *141*, 235–264, doi:10.1007/s11214-008-9365-9.

Bale, S. D., C. J. Owen, J.-L. Bougeret, K. Goetz, P. J. Kellogg, R. P. Lepping, R. Manning, and S. J. Monson (1997), Evidence of currents and unstable particle distributions in an extended region around the lunar plasma wake, *Geophys. Res. Lett.*, *24*(11), 1427–1430, doi:10.1029/97GL01193.

Birch, P. C., and S. C. Chapman (2001), Particle-in-cell simulations of the lunar wake with high phase space resolution, *Geophys. Res. Lett.*, *28*(2), 219–222, doi:10.1029/2000GL011958.

Clack, D., J. C. Kasper, A. J. Lazarus,J. T. Steinberg, and W. M. Farrell (2004), Wind observations of extreme ion temperature anisotropies in the lunar wake, *Geophys. Res. Lett.*, *31*, L06812, doi:10.1029/2003GL018298.

Colburn, D. S., R. G. Currie, J. D. Mihalov, and C. P. Sonett (1967), Diamagnetic solar-wind cavity discovered behind moon, *Science*, *158*, 1040–1042, doi:10.1126/science.158.3804.1040.

England, A. W., G. Simmons, and D. Strangway (1968), Electrical conductivity of the Moon, *J. Geophys. Res.*, *73*(10), 3219–3226, doi:10.1029/JB073i010p03219.

Farrell, W. M., M. L. Kaiser, and J. T. Steinberg (1997), Electrostatic instability in the central lunar wake: A process for replenishing the plasma void, *Geophys. Res. Lett.*, *24*(9), 1135–1138, doi:10.1029/97GL00878.

Farrell, W. M., M. L. Kaiser, J. T. Steinberg, and S. D. Bale (1998), A simple simulation of a plasma void: Applications to wind observations of the lunar wake, *J. Geophys. Res.*, *103*, 23,653–23,660, doi:10.1029/97JA03717.

Fatemi, S., M. Holmstrom, and Y. Futaana (2012), The effects of lunar surface plasma absorption and solar wind temperature anisotropies on the solar wind proton velocity space distributions in the low-altitude lunar plasma wake, *Geophys. Res.*, *117*, A10105, doi:10.1029/2011ja017353.

Fatemi, S., M. Holmstrom, Y. Futaana, S. Barabash, and C. Lue (2013), The lunar wake current systems, *Geophys. Res. Lett.*, *40*, 17–21, doi:10.1029/2012GL054635.

Halekas, J. S., S. D. Bale, D. L. Mitchell, and R. P. Lin (2005), Magnetic fields and electrons in the lunar plasma wake, *J. Geophys. Res.*, *110*, A07222, doi:10.1029/2004JA010991.

Halekas, J. S., G. T. Delory, D. A. Brain, R. P. Lin, and D. L. Mitchell (2008), Density cavity observed over a strong lunar crustal magnetic anomaly in the solar wind: A mini-magnetosphere, *Planet. Space Sci.*, *56*(7), 941–946.

Halekas, J. S., Y. Saito, G. T. Delory, and W. M. Farrell (2011), New views of the lunar plasma environment, *Planet. Space Sci.*, *59*(14), 1681–1694.

Hoffman, J. H., R. R. Hodges Jr., F. S. Johnson, and D. E. Evans (1973), Lunar atmospheric composition results from Apollo 17, Proceedings of the 4th Lunar Science Conference, 2865-2875.

Holmstrom, M., S. Fatemi, Y. Futaana, and H. Nilsson (2012), The interaction between the Moon and the solar wind, *Earth Planets Space*, *64*, 237–245.

Johnson, F., and J. E. Midgley (1968), Notes on the lunar magnetosphere, *J. Geophys. Res.*, *73*(5), 1523–1532, doi:10.1029/JA073i005p01523.

Kallio, E. (2005), Formation of the lunar wake in quasi-neutral hybrid model, *Geophys. Res. Lett.*, *32*, L06107, doi:10.1029/2004GL02198.

Kellogg, P. J., K. Goetz, S. J. Monson, J.-L. Bougeret, R. Manning, and M. L. Kaiser (1996), Observations of plasma waves during a traversal of the Moon's wake, *Geophys. Res. Lett.*, *23*(10), 1267–1270, doi:10.1029/96GL00376.

Khurana, K. K., C. T. Russell, and M. K. Dougherty (2008), Magnetic portraits of Tethys and Rhea, *Icarus*, *193*, 465–474, doi:10.1016/j.icarus.2007.08.005.

Lyon, E. F., H. S. Bridge, and J. H. Binsack (1967), Explorer 35 plasma measurements in the vicinity of the Moon, *J. Geophys. Res.*, *72*(23), 6113–6117, doi:10.1029/JZ072i023p06113.

McFadden, J. P., C. W. Carlson, D. Larson, M. Ludlam, R. Abiad, B. Elliott, P. Turin, M. Marckwordt, and V. Angelopoulos (2008), The THEMIS ESA plasma instrument and in-flight calibration, *Space Sci. Rev.*, *141*, 277–302, doi:10.1007/s11214-008-9440-2.

Michel, F. C. (1968), Magnetic field structure behind the Moon, *J. Geophys. Res.*, *73*(5), 1533–1542, doi:10.1029/JA073i005p01533.

Nakagawa, T. (2013), Ion entry into the wake behind a nonmagnetized obstacle in the solar wind: Two-dimensional particle-in-cell simulations, *J. Geophys. Res. Space Physics*, *118*, 1849–1860.

Ness, N. F., K. W. Behannon, C. S. Searce, and S. C. Cantarano (1967), Early results from the magnetic field experiment on lunar Explorer 35, *J. Geophys. Res.*, *72*(23), 5769–5778, doi:10.1029/JZ072i023p05769.

Ness, N. F., K. W. Behannon, H. E. Taylor, and Y. C. Whang (1968), Perturbations of the interplanetary magnetic field by the lunar wake, *J. Geophys. Res.*, *73*(11), 3421–3440, doi:10.1029/JA073i011p03421.

Ogilvie, K. W., and N. F. Ness (1969), Dependence of the lunar wake on solar wind plasma characteristics, *J. Geophys. Res.*, *74*, 4123–4128, doi:10.1029/JA074i016p04123.

Ogilvie, K. W., J. T. Steinberg, R. J. Fitzenreiter, C. J. Owen, A. J. Lazarus, W. M. Farrell, and R. B. Torbert (1996), Observations of the lunar plasma wake from the WIND spacecraft on December 27, 1994, *Geophys. Res. Lett.*, *23*(10), 1255–1258, doi:10.1029/96GL01069.

Owen, C. J., R. P. Lepping, K. W. Ogilvie, J. A. Slavin, W. M. Farrell, and J. B. Byrnes (1996), The lunar wake at 6.8 R_L: WIND magnetic field observations, *Geophys. Res. Lett.*, *10*, 1263–1266, doi:10.1029/96GL01354.

Rennilson, J. J., and D. R. Criswell (1974), Surveyor Observations of Lunar Horizon-Glow, *Earth, Moon, and Planets*, *10*(2), 121–142.

Roussos, E., J. Mueller, S. Simon, A. Boesswetter, U. Motschmann, N. Krupp, M. Fraenz, J. Woch, K. K. Khurana, and M. K. Dougherty (2008), Plasma and fields in the wake of Rhea: 3-D hybrid simulation and comparison with Cassini data, *Ann. Geophys.*, *26*(3), 619–637.

Russell, C. T. (1993), Magnetic fields of the terrestrial planets, *J. Geophys. Res.*, *98*(10), 18,681–18,695, doi:10.1029/93JE00981.
Samir, U., K. H. Wright Jr., and N. H. Stone (1983), The expansion of a plasma into a vacuum: Basic phenomena and processes and applications to space plasma physics, *Rev. Geophys.*, *21*, 1631–1646, doi:10.1029/RG021i007p01631.
Sibeck, D. G., et al. (2011), ARTEMIS science objectives, *Space Sci. Rev.*, *165*, 59–91, doi:10.1007/s11214-011-9777-9.
Sonett, C. P., D. S. Colburn, and R. G. Currie (1967), The intrinsic magnetic field of the Moon, *J. Geophys. Res.*, *72*(21), 5503–5507, doi:10.1029/JZ072i021p05503.
Spreiter, J. R., A. L. Summers, and A. W. Rizzi (1970), Solar wind flow past nonmagnetic planets—Venus and Mars, *Planet. Space Sci.*, *18*(9), 1281–1299.
Stubbs, T. J., R. R. Vondrak, and W. M. Farrell (2006), A dynamic fountain model for lunar dust, in *Moon and Near-Earth Objects*, edited by P. Ehrenfreund, B. Foing, and A. Cellino, pp. 59–66, Elsevier Science Bv, Amsterdam, Netherlands.
Travnicek, P., P. Hellinger, D. Schriver, and S. D. Bale (2005), Structure of the lunar wake: Two-dimensional global hybrid simulations, *Geophys. Res. Lett.*, *32*, L06102, doi:10.1029/2004GL022243.
Vernisse, Y., H. Kriegel, S. Wiehle, U. Motschmann, and K.-H. Glassmeier (2013), Stellar winds and planetary bodies simulations: Lunar type interaction in super-Alfvenic and sub-Alfvenic flows, *Planet. Space Sci.*, *84*, 37–47.
Wang, Y. C., J. Muller, W.-H. Ip, and U. Motschmann (2011), A 3D hybrid simulation study of the electromagnetic field distributions in the lunar wake, *Icarus*, *216*(2), 415–425.
Whang, Y. C. (1968a), Interaction of the magnetized solar wind with the Moon, *Phys. Fluids*, *11*, 969–975.
Whang, Y. C. (1968b), Theoretical study of the magnetic field in the lunar wake, *Phys. Fluids*, *11*, 1713–1719.
Whang, Y. C. (1970), Two-dimensional guiding-center model of the solar wind-moon interaction, *Solar Phys.*, *14*(2), 489–502, doi:10.1007/BF00221333.
Whang, Y. C., and N. F. Ness (1970), Observations and interpretation of lunar mach cone, *J. Geophys. Res.*, *75*(31), 6002–6010, doi:10.1029/JA075i031p06002.
Wiehle, S., et al. (2011), First lunar wake passage of ARTEMIS: Discrimination of wake effects and solar wind fluctuations by 3D hybrid simulations, *Planet. Space Sci.*, *59*, 661–671.
Wolf, R. A. (1968), Solar-wind flow behind the Moon, *J. Geophys. Res.*, *73*(13), 4281–4289, doi:10.1029/JA073i013p04281.
Xie, L. H., L. Li, Y. T. Zhang, and D. L. De Zeeuw (2013), Three-dimensional MHD simulation of the lunar wake, *Sci. Chin. Earth Sci.*, *56*(2), 330–338.
Zhang, H., et al. (2012), Outward expansion of the lunar wake: ARTEMIS observations, *Geophys. Res. Lett.*, *39*, L18104, doi:10.1029/2012GL052839.